Monthly Notices
of the
ROYAL ASTRONOMICAL SOCIETY

MNRAS **478,** 3199–3219 (2018) doi:10.1093/mnras/sty1026
Advance Access publication 2018 April 26

OJ287: deciphering the '*Rosetta* stone of blazars⋆'

S. Britzen,[1]† C. Fendt,[2] G. Witzel,[3] S.-J. Qian,[4] I. N. Pashchenko,[5] O. Kurtanidze,[6,7] M. Zajacek,[1,8,10] G. Martinez,[3] V. Karas,[8] M. Aller,[9] H. Aller,[9] A. Eckart,[1,10] K. Nilsson,[11] P. Arévalo,[12] J. Cuadra,[13] M. Subroweit[10] and A. Witzel[1]

[1]*Max-Planck-Institut für Radioastronomie, Auf dem Hügel 69, D-53121 Bonn, Germany*
[2]*Max-Planck-Institut für Astronomie, Königstuhl, D-69117 Heidelberg, Germany*
[3]*UCLA, Department of Physics and Astronomy, LA, CA 90095, USA*
[4]*National Astronomical Observatories, Chinese Academy of Sciences, Beijing 100012, China*
[5]*Astro Space Center, Lebedev Physical Institute, Russian Academy of Sciences, 84/32 Profsoyuznaya st., Moscow, GSP-7, 117997, Russia*
[6]*Abastumani Observatory, Mt Kanobili, 0301 Abastumani, Georgia*
[7]*Engelhard Astronomical Observatory, Kazan Federal University, 422526 Tatarstan, Russia*
[8]*Astronomical Institute, Academy of Sciences, Boční II 1401, CZ-14131 Prague, Czech Republic*
[9]*University of Michigan, Ann Arbor, MI 48109, USA*
[10]*I. Physikalisches Institut der Universität zu Köln, Zülpicher Str 77, D-50937 Köln, Germany*
[11]*Tuorla Observatory, Department of Physics and Astronomy, University of Turku, FI-20500 Turku, Finland*
[12]*Instituto de Física y Astronomía, Facultad de Ciencias, Universidad de Valparaíso, Gran Bretaña No. 1111, Playa Ancha, 2360102 Valparaíso, Chile*
[13]*Instituto de Astrofísica, Pontificia Universidad Católica de Chile, 782-0436 Santiago, Chile*

Accepted 2018 April 19. Received 2018 April 19; in original form 2017 September 7

ABSTRACT

OJ287 is the best candidate active galactic nucleus (AGN) for hosting a supermassive binary black hole (SMBBH) at very close separation. We present 120 Very Long Baseline Array (VLBA) observations (at 15 GHz) covering the time between April 1995 and April 2017. We find that the OJ287 radio jet is precessing on a time-scale of ∼22 yr. In addition, our data are consistent with a jet-axis rotation on a yearly time-scale. We model the precession (24 ± 2 yr) and combined motion of jet precession and jet-axis rotation. The jet motion explains the variability of the total radio flux-density via viewing angle changes and Doppler beaming. Half of the jet-precession time-scale is of the order of the dominant optical periodicity time-scale. We suggest that the optical emission is synchrotron emission and related to the jet radiation. The jet dynamics and flux-density light curves can be understood in terms of geometrical effects. Disturbances of an accretion disc caused by a plunging BH do not seem necessary to explain the observed variability. Although the SMBBH model does not seem necessary to explain the observed variability, an SMBBH or Lense-Thirring precession (disc around single BH) seem to be required to explain the time-scale of the precessing motion. Besides jet rotation also nutation of the jet axis could explain the observed motion of the jet axis. We find a strikingly similar scaling for the time-scales for precession and nutation as indicated for SS433 with a factor of roughly 50 times longer in OJ287.

Key words: black hole physics – techniques: interferometric – BL Lacertae objects: individual: OJ287.

1 INTRODUCTION

OJ287 is a prototypical active galactic nucleus (AGN) which is well-known for rather pronounced and specific properties. The source has been named the *Rosetta* stone of blazars (Takalo 1994) and the hope is, that by deciphering this particular blazar, we will be able to better understand the AGN phenomenon in general. OJ287 [z= 0.306; Stickel, Fried & Kühr 1989; low synchrotron peaked (LSP) BL Lac Object] has been claimed to be the most promising AGN for hosting a supermassive binary black hole (SMBBH) at the centre. A light-curve observed in the optical V band since 1890 shows repeated outbursts at ∼11.65 yr intervals of this object (Sillanpää et al. 1988). Since the light curve during an outburst resembles the pattern of inflow of gas from an accretion disc to a supermassive BH in a

† E-mail: sbritzen@mpifr.de
⋆ Takalo (1994).

tidal perturbation, Sillanpää et al. (1988) proposed that OJ287 is a binary pair of SMBHs with an orbital period of 9 yr in the rest frame of OJ287. They also claimed that the light variations are related to tidally induced mass flows from accretion discs into black holes (BHs). Lehto & Valtonen (1996) analysed the substructure inside the major outbursts and identified well-defined sharp flares. They explain these with a model in which a smaller BH crosses the accretion disc of a larger BH during the binary orbit of the BHs about each other. Sundelius et al. (1996) modelled the binary BH, assuming one supermassive object orbits around a second in a precessing orbit that intersects the accretion disc surrounding it. Sundelius et al. (1997) present numerical simulations of a model where the observed major outbursts are identified with the pericentre passages of the secondary BH, while the super-flares are identified with its disc crossings. Their simulations generate a light curve from a disc of particles interacting with the BHs. They predict the outburst in 1995–1996. Further works by Lehto & Valtonen (1996) and Valtonen et al. (2012, 2016) have explored the binary BH nature of this AGN. Valtonen et al. (2016) use *Swift*/XRT satellite measurements together with optical polarization data to determine the spin of the primary BH based on the last major optical outburst in December 2015. The spin is determined to be $\chi = 0.313 \pm 0.01$. The authors also find that this outburst confirms the established general relativistic properties of the system (Valtonen & Lehto 1997; Valtonen et al. 2010) such as the loss of orbital energy to gravitational radiation at the 2 per cent accuracy level. In addition, the authors mention that the BH no-hair theorem might be tested with 10 per cent accuracy during the present decade.

The scope of this paper:

So far, it has proved difficult to relate the flaring variability observed in the optical wavelength regime for OJ287 with the flaring variability observed in the radio on the one hand, and the morphological changes of the pc-scale radio jet on the other hand. In particular, an important question relates to the nature of the radio jet emission and the jet direction – does this really change erratically as the results by Agudo et al. (2012) suggest? Can the radio jet direction and its changes tell us more about the origin of the jet? Is the origin (or launching of the jet) effected by the plunging scenario (Valtonen et al. 2016)? In this paper, we investigate these relations and discuss the consequences for our understanding of the physical processes driving OJ287. OJ287 indeed seems to be a prototypical object. Our findings might thus have more far-reaching consequences.

Throughout the paper we adopt the following parameters: a luminosity distance $D_{\rm L} = 1.592$ Gpc, at the source redshift of $z = 0.306$, with cosmological parameters corresponding to a ΛCDM of the Universe with $\Omega_m = 0.3$, $\Omega_\lambda = 0.7$, and $H_0 = 70\,{\rm km\,s^{-1}\,Mpc^{-1}}$. A proper motion of 1 mas yr^{-1} corresponds to an apparent superluminal speed of $14.7c$. 1 mas = 4.521 pc.

1.1 The mass of the BH in OJ287

There have been several attempts to determine the mass of OJ287 based on optical and infrared observations. The host galaxy of OJ287 is difficult to resolve; the magnitude and morphology of the host galaxy remained ambiguous for a long time. Wright, McHardy & Abraham (1998) fit optical data by the Canada–France–Hawaii Telescope (CFHT). They find that the galaxy (i.e. either elliptical or disc) plus core model does not fit the data better than a pure core fit. They thus cannot prove the detection of a galaxy but their fitted galaxy magnitude provides a reasonable approximation to the upper limit on the flux from any host galaxy present. One-dimensional modelling of their near-infrared observations (taken with WHIRCAM) detects extended galaxy emission in one of four images obtained (*K* band). The authors cannot ascribe a morphology to the host galaxy of OJ287. Higher resolution, deeper *K*-band images are required. Heidt et al. (1999) marginally resolved the host galaxy of OJ287 with an effective radius $r_{\rm e}$= 0.72 arcsec and an absolute magnitude $M_R = -23.23$.

Gebhardt et al. (2000) and Merritt & Ferrarese (2001a,b) found a tight correlation between the masses of the centre BHs in active and inactive galaxies and the bulge velocity dispersion. Magorrian et al. (1998) and McLure & Dunlop (2002) found a similar relation between the masses of the BHs and the bulge luminosities.

Liu & Wu (2002) calculate a BH mass of $M \simeq 4.6 \times 10^8\,{\rm M}_\odot$ with the absolute magnitude and the correlation between the BH mass and bulge luminosity ($M - {\rm L_{bulge}}$) for active galaxies by McLure & Dunlop (2002). Liu & Wu (2002) derived the BH mass of OJ287 by making use of the velocity dispersion σ and the M–σ correlation by Merritt & Ferrarese (2001b). They used the morphological data of the host galaxy by Heidt et al. (1999) and estimated the central velocity dispersion σ by making use of the Fundamental Plane of tight correlations between the velocity dispersion, the effective radius and the average surface brightness for elliptical galaxies by Bettoni (2001). Liu & Wu (2002) derive a second BH mass of $M \simeq 3.2 \times 10^8\,{\rm M}_\odot$. A BH mass of the order of $10^8\,{\rm M}_\odot$ fits into the distribution of BH masses derived by Plotkin et al. (2011) for BL Lac Objects from the Sloan Digital Sky Survey. Valtonen et al. (2012) used two multifrequency campaigns of OJ287 (2005) from radio to X-ray observations and the estimate on the bremsstrahlung radiation, which arises from a hot bubble of gas torn off the accretion disc by the impact of the secondary, to determine the mass of the secondary BH ($\sim 1.4 \times 10^8\,{\rm M}_\odot$). From stability arguments of the accretion disc and particle simulations they find the ratio between the two masses to be $\sim 1.3 \times 10^2$. The minimum mass of the primary results to be $\sim 1.8 \times 10^{10}\,{\rm M}_\odot$. Valtonen et al. (2016) determined the BH masses to be $(1.83 \pm 0.01) \times 10^{10}\,{\rm M}_\odot$ (primary BH) and $(1.5 \pm 0.1) \times 10^8\,{\rm M}_\odot$ (secondary BH). A primary BH with a mass of about $M_{\rm p} = 1.8 \times 10^{10}\,{\rm M}_\odot$ hits an upper limit for the maximum observable mass of the SMBBH, estimated to be $M_{\rm max} \approx 5 \times 10^{10}\,{\rm M}_\odot$ (King 2016).

Two different mass scales have been determined for OJ287 – either about $10^8\,{\rm M}_\odot$ (Liu & Wu 2002) or about $10^{10}\,{\rm M}_\odot$ (Valtonen et al. 2016). We discuss both masses: $10^8\,{\rm M}_\odot$ as input parameter for our models in Section 6 and $10^{10}\,{\rm M}_\odot$ in Section 6.4 to compare our results with the Valtonen model.

1.2 Periodicities in the light curves (radio and optical)

The optical light curve of OJ287 displays different types of variability. The strongest flares of more than 3 mag in the *V* band have a duration of a few months and almost constant colour indices and similar temporal behaviour (Sillanpää et al. 1985). They repeat with a periodicity of about 11.6 yr (Sillanpää et al. 1988, 1996). The very strong periodic optical flares do not seem to have counterparts in the radio region according to Valtaoja (1996). Hughes, Aller & Aller (1998) performed a detailed study of the radio variability using wavelet analysis and found a periodicity of 1.66 yr in the complete data series and for another signal that dominates the activity in the 1980s with a period of about 1.12 yr close to the epoch of the 1983 optical flare. Hovatta et al. (2008) investigated the long-term radio monitoring at 22, 37, and 90 GHz of the Metsähovi Radio Observatory. The wavelet analysis yields a period of 1.4 yr at 22 and 90 GHz, and a period of 1.7 yr at 37 GHz. Donskykh (2016)

studies the long-term monitoring data of the UMRAO programme at 14.5, 8.0, and 14.5 GHz obtained during 40 yr by applying the wavelet and the singular spectrum methods. The wavelet analysis at all frequencies revealed the presence of quasi-periods within the intervals of 6.0–7.4 and 1.2–1.8 yr. The singular spectrum analysis revealed the presence of quasi-periods within the intervals of 6–10 and 1.6–4.0 yr. The results dominating the different analysis is a time-scale of roughly 12 yr in the optical domain and of a bit more than 1 yr in the radio domain. There is some evidence for another time-scale in the radio data of around 6–7 yr.

1.3 The jet of OJ287 in VLBI observations

OJ287 has been frequently studied at several frequencies and with different radio interferometric arrays. At parsec scales, it reveals a compact one-sided core-jet structure. Moderate apparent superluminal velocities in the 3 mas long jet have been discovered at 5 and 8.4 GHz by several authors. Gabuzda, Wardle & Roberts (1989) determine proper motions of 0.20 ± 0.03 and 0.27 ± 0.03 mas yr^{-1} corresponding to $\beta_{\rm app}h = 2.4 \pm 0.4$ and $\beta_{\rm app}h = 3.2 \pm 0.4$ (with $H_0 = 100h$ km s^{-1}). Gabuzda & Cawthorne (1996) confirm the results of Gabuzda et al. (1989) in four-epoch apparent speeds of $\beta_{\rm app}h = 2.6 \pm 0.2$ and $\beta_{\rm app}h = 3.2$. Vicente, Charlot & Sol (1996) find the coexistence of both moving and stationary components and a deceleration of a knot (K3). Proper motion values range between $\sim$0.2 and $\sim$0.4 mas yr^{-1}, similar to those found earlier.

Tateyama & Kingham (2004) studied the Radio Reference Frame Image Database data of the US Naval Observatory (USNO) at 8 GHz of OJ287. The data comprise VLBA observations made between 1994 and 2002. The position angle of the more collimated unresolved jet rotated clockwise by $\sim$30° in 8 yr that can be explained within a ballistic precessing model. The aperture angle of the precessing cone is 3°, the axis of the precessing cone forms an angle of 11° with the line of sight and has a projected position angle of −107° in the plane of the sky. OJ287 was studied as part of the MOJAVE[1] (Monitoring Of jets in Active galactic nuclei with VLBA Experiments) survey, e.g. Hovatta et al. (2014); Lister et al. (2009, 2013). Tateyama (2013) investigated the inner jet of OJ287 in VLBA observations (15 GHz) within the MOJAVE programme in super-resolution mode (the restoring beam was 0.1 mas). The jet is in the form of a 'fork' where superluminal components emerge via stationary components at the north-west and the south-east close to the core to form parallel trajectories along the southwest direction in the plane of the sky. Agudo et al. (2012) analysed 136 images from an ultra-high-resolution 43 GHz VLBA study of the relativistic jet in OJ287 from 1995 to 2011. A sharp jet-position-angle swing by >100° during [2004, 2006] is found, as viewed in the plane of the sky, which they interpret as the crossing of the jet from one side of the line of sight to the other during a softer- and longer-term swing of the inner jet. Prominent erratic wobbling behaviour of the innermost $\sim$0.4 mas of the jet with fluctuations in position angle of up to $\sim$40° over time-scales of $\sim$2 yr is found, accompanied by highly superluminal motions along non-radial trajectories. Agudo et al. (2012) claim that the erratic nature and short time-scales of the observed behaviour rule out scenarios such as binary BH systems, accretion disc precession, and interaction with the ambient medium as possible origins of the phenomenon on the scales probed by their observations, although such processes may cause longer-term modulation of the jet direction. Agudo et al. (2012) propose that variable asymmetric injection of the jet flow, perhaps related to turbulence in the accretion disc, coupled with hydrodynamic instabilities leads to the non-ballistic dynamics that causes the observed non-periodic changes in the direction of the inner jet. Hodgson et al. (2017) investigated the location of γ-ray emission and magnetic field strength in OJ287. They find that strong γ-ray flares either originate from the core region, a downstream stationary feature, or both. Recently, Cohen (2017) presented evidence for OJ287 as a rotating helix. He investigated 15 GHz VLBA images from 1995 to 2015. Based on the analysis of the ridge lines, the author suggests that the jet is rotating with a period of possibly $\sim$30 yr. The inner jet apparently seems to have moved to a new direction after the rotation. A model of a helical jet being observed from a small and varying viewing angle had been proposed earlier by Valtonen & Pihajoki (2013).

[1] www.physics.purdue.edu/astro/MOJAVE/

2 OBSERVATIONS AND DATA REDUCTION

We re-modelled and re-analysed 120 VLBA observations (15 GHz, MOJAVE) performed between April 1995 and April 2017. Gaussian circular components were fitted to the data to obtain the optimum set of parameters within the *difmap*-modelfit program (Shepherd 1997). Several identification schemes were tested to most reliably trace the components through the epochs. Special care was taken to correctly identify the core component in every individual data set. To ensure that the proper component was chosen, we selected this component based on the assumption, that the transition with regard to the parameters 'radial distance' as well as 'position angle' from one epoch to the next epoch should be as smooth as possible. We further assume that 'erratic wobbling' or 'jumps' in the position of jet components are unlikely to happen between two epochs that are close in time. At the scales on which we study the jet, we consider a smooth transition between the jet component positions from one epoch to the next epoch to be the most physical and reliable one. All maps with modelfit components superimposed are shown in Figs A1–A8. Uncertainties of the modelfit component parameters were determined using *bootstrap* (Efron 1979). For bootstrap applications to estimate uncertainties of VLBI results, see Pashchenko (2017). We bootstrapped the adjusted residuals between self-calibrated interferometric visibilities and the best-fitting *difmap* model. The residuals were first filtered from outliers, centred and distributions of the adjusted residuals were fitted using kernel density estimates (KDE). It was done independently for each baseline, correlation, and frequency sub-band. We then added samples of the residuals from the fitted KDE to the model visibilities obtained from our best *difmap* model. The resulting 'bootstrapped' visibility data sets were fitted in *difmap* using the original best-fitting model as the initial guess. This was done 300 times for each epoch. Thus, we obtained a distribution for each parameter. The standard deviation was used for estimating the corresponding uncertainty. The parameters of the fitted Gaussian components and their associated errors are listed in Table B1 (the full table is available online). **C1–C14** denote for the identified fast components (discussed later in this paper), **a–c** for the identified stationary components, ***k*** for the core, and ***x*** for the identified counter-jet components.

The single-dish radio flux-density data at three frequencies (4.8, 8.0, 14.5 GHz) have been obtained within the University of Michigan (UMRAO) monitoring programme. The data are shown in Fig. 6 (top three panels). To analyse the optical data, we combined historical light-curve information with data taken by the Abastumani Observatory. The latter were obtained in *R* band (Cousins) using the 70-cm meniscus (f/3, SBIG ST6, and Apogee Ap6E) and 125-cm Ritchey-Chretien (f/13, Apogee Ap6E) telescopes. At least three to

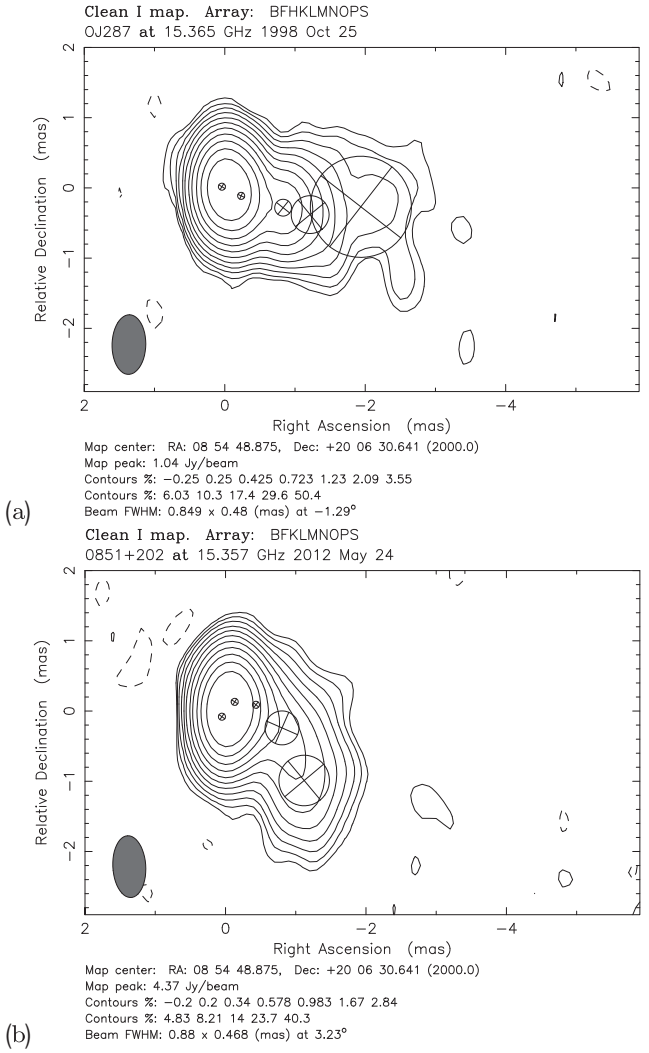

Figure 1. Images with model-fit components superimposed showing the basic structure of the pc-scale jet of OJ287 before 2010 (a) and after the significant change in morphology (b). Not only the morphology changed but also the kinematics of the jet changed (see the text).

four images were obtained during the night (one pointing) and typical exposures are between 1 and 3 min depending on the brightness of the source. The frames after pre-processing (dark subtraction, cosmic ray removal, and flat fielding) have been reduced using DaoPhot II. The magnitudes were integrated within an aperture of 10 arcsec diameter and calibrated with five calibration stars in the direct vicinity of OJ287 (comparison stars from Fiorucci & Tosti 1996). We then converted the magnitudes to flux densities using zero-point fluxes of Bessel, Castelli & Plez (1998) (B: 4063 Jy, V: 3064 Jy, R: 3064 Jy, I: 2416 Jy). The optical data are shown in Fig. 6(a) (bottom panel) and (b).

3 RESULTS OF THE VLBA DATA ANALYSIS

The VLBI morphology of the pc-scale jet OJ287 evolves significantly in time. Around 2010, a drastic change in the VLBI structure occurs. We show two representative images of the time before 2010 (a) and after 2010 (b) in Fig. 1. The jet components appear at significantly different position angles. In the following, we discuss our results in detail.

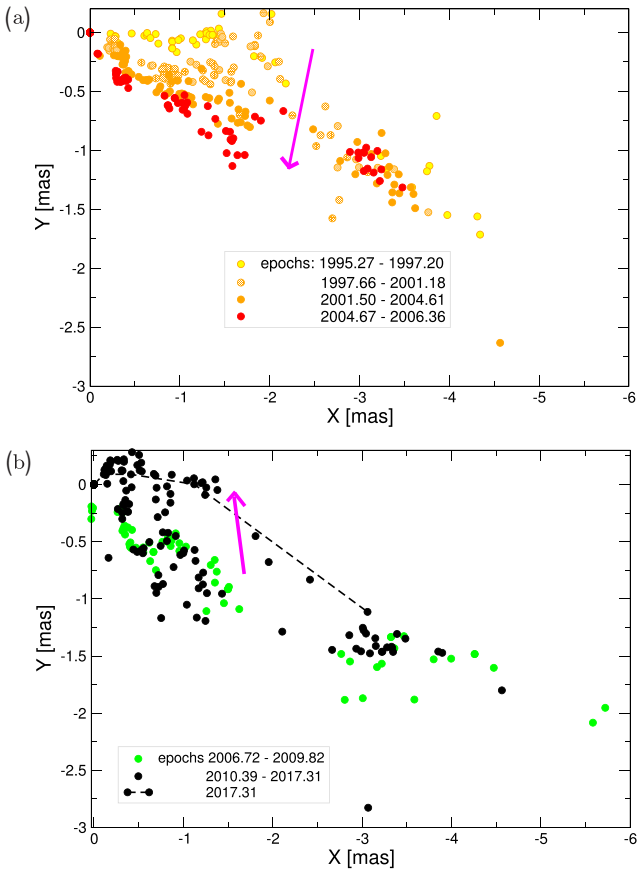

Figure 2. Jet precession. We plot all the (*X*, *Y*) data points of the 120 re-analysed epochs. The counter-jet components have been deliberately taken out. The sequence of the combined effect of rotation and precession starts in time in (a) with the earliest data (yellow). We indicate the motion and evolution in time with different colours. (b) is a continuation of (a). The light-green data continue with a 'jump' to the black filled circles in (b). In both plots an arrow (magenta) indicates the main direction of the projected jet precession motion. In (a) the dominant motion is downward. In (b) the dominant motion is upward. The dashed line in (b) indicates the most recently observed jet ridge line which seems to coincide with the position of the oldest jet ridge lines (yellow) shown in (a). Thus, we think we observe a full precession orbit.

3.1 Jet kinematics

We find that the jet and the jet components of OJ287 are moving in a complex way. In the following, we describe and discriminate between the different aspects of motion.

3.1.1 Jet ridge line motion on long time-scales (∼22 yr)

The 'ridge line' as we use it in this manuscript connects all jet features modelled per Gaussian components per epoch. We traced the evolution of these ridge lines through all the epochs. The ridge line is a sequence of all the Gaussian components (per epoch) with regard to their increasing distance from the core. The ridge line evolution is shown in both figures of Fig. 2. To better indicate how the jet moves in the plane of the sky, we mark different periods of time (comprising several epochs) of data by different colours. Fig. 2(a) shows the earlier data (from 1995.27 to 2006.36) and (b) the ridge line evolution in later epochs (from 2006.72 to 2017.31).

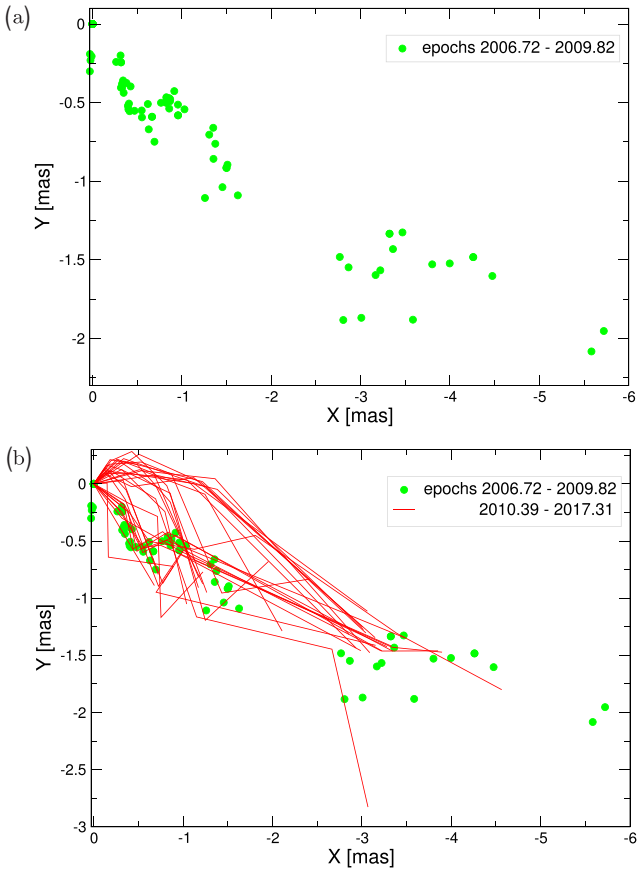

Figure 3. Helix. (a) shows in more detail the data points of the time 2006.72–2009.82. The data show the signature of a projected helix. (b) is the same as (a) but in addition the epochs 2010.39–2016.46 are plotted as lines (red). This might give a better impression of the motion that is taking place.

The earlier data show how the jet in the plane of the sky 'moves' downwards (arrow in magenta indicates the direction of the motion). The later data show an upward trend (again indicated by an arrow in magenta) which starts after epoch 2009.82. We assume that the jet motion changed direction and allows a more direct view into the jet (smaller angle to the line of sight). Comparing the earliest jet ridge line of the here analysed data in Fig. 2(a) with the latest jet ridge line in Fig. 2(b), we find that they appear at similar *xy*-coordinates [please compare the yellow filled circles in (a) with the black dashed line in (b)]. It thus seems that we might witness a periodic process with a time-scale of roughly 22 yr. We suggest that motion seen in the *xy*-plots of the ridge lines can best be explained by a precession of the radio jet in the plane of the sky.

To show this long time-scale motion in more detail, we provide further figures. Fig. 3(a) displays all data points in the period between 2006.72 and 2009.82. The data points clearly indicate the shape of a helix in projection. The helix develops along the whole jet line simultaneously and every epoch adds new data points at different parts along the jet. It is this helix which we see under different viewing angles as the jet moves in the sky. Fig. 3(b) shows the same data as Fig. 2(a). To better see the difference between different jet structures, we connect all data points per epoch with lines. Red lines indicate the most recent jet-data.

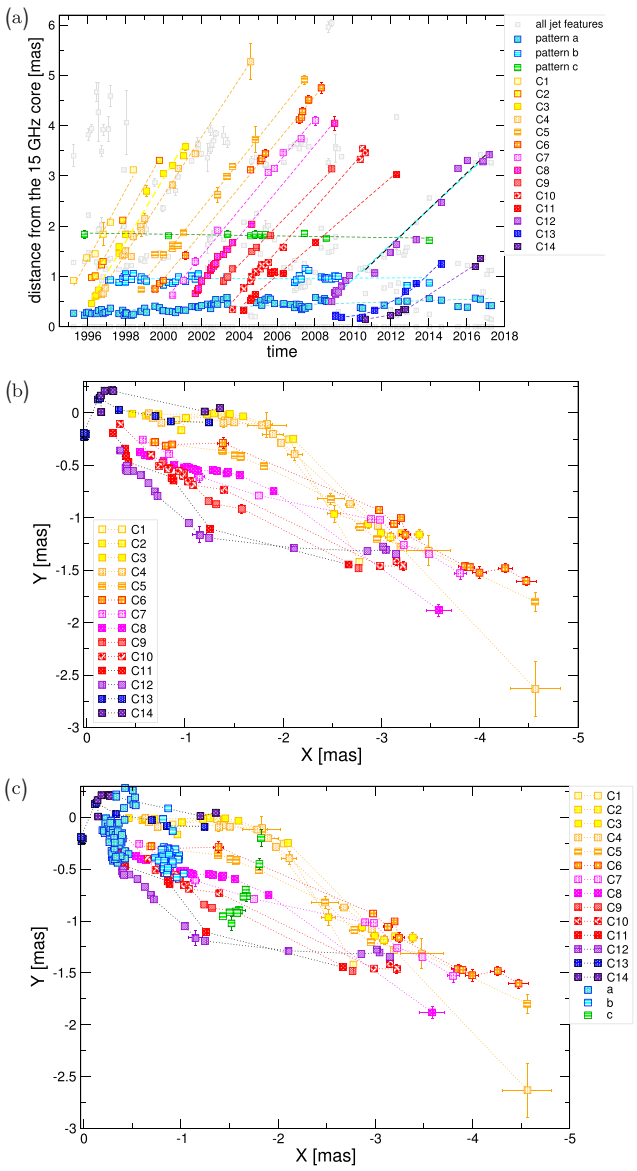

Figure 4. The distance between the 15 GHz core and the jet components plotted as function of time (a). Individual jet components are shown in different colours. For components up to **C12** the linear regression line is superimposed. For components **C13** and **C14**, a quadratic fit has been applied (see the text for details). (b) shows the components **C1**–**C14** in *xy*-coordinates. Both figures have been prepared with the counter-jet components deliberately left out. (c) shows the same relation as in (b) but with those stationary components superimposed that do seem to remain at similar core separations.

3.1.2 Jet component motion: fast and stationary components

The core separation versus time plot (Fig. 4a) is the standard tool to determine the apparent speeds of jet components. The plot is dominated by stationary and moving features before 2010. The stationary features do not reveal significant motion away from the core and are shown in Fig. 4(a) as **a**, **b**, and **c**. **a** is found at a core separation of 0.3–0.5 mas, **b** is found at ∼1 mas distance from the core, and **c** at a core separation of ∼1.8 mas. The apparent speeds have been determined via linear regression for all but components **C13** and **C14**. Linear regression was performed on the radial distance as function of time for components **C1**–**C12**. Please note that components

C1–C12 in *xy*-coordinates move on bent paths (as is shown in Fig. 4b). For the apparent speed determination, the bent paths have not been taken into account. For components **C13** and **C14**, quadratic fits have been applied to the data. Component identification is less certain for **C13** and **C14** since more data would be required. The component speeds and ejection times are listed in Table 1. As can be seen from Table 1, the apparent speeds are (almost continuously) decreasing from **C1** to **C11**. Consequently, the viewing angle is increasing between 5.5 and 12.0 deg for the earliest appearing jet feature **C1** to **C11**. The viewing angle has been determined based on the assumption that the jet has the minimum Lorentz factor required to achieve the observed apparent velocity of the component. This is explained in more detail in Section 5. With regard to the kinematics of the jet components in OJ287, we find the following jet component motions:

(i) *Fast moving features* – These (in the core separation plot) do reveal fast radial outward motion with apparent superluminal motion with respect to the core. These are jet components **C1–C14**. The motion in *xy*-coordinates is shown in Fig. 4(b).

(ii) *Stationary features* – These (in the core separation plot) do not reveal significant radial outward motion with respect to the core. These components are **a**, **b**, and **c**. They are shown in Fig. 4(a) and superimposed on the *xy*-plot in Fig. 4(c). These jet features remain at similar distances from the core but move in perpendicular direction to the jet axis (see Fig. 4c). Significant motion can be traced with regard to the position angle. The most prominent stationary feature, due to its brightness, is component **a** in OJ287.

3.1.3 Jet component motion on short time-scales (∼1 yr)

In addition to the motion of the jet ridge line in the *xy*-plane on a time-scale of about 22 yr, and in addition to the outwards directed motion of the fast jet components, we find some indication for another superimposed motion perpendicular to the jet axis. In Fig. 5, we show that the stationary feature component **a**, while remaining at the same core separation, moves up and down with regard to the *y*-component with time (in Fig. 5b). This kind of motion occurs repeatedly and is shown for the complete data set of component **a** in Fig. 12. The time-scale of motion is of the order of 1–1.4 yr and could be consistent with rotation. The time-scale of this motion can be determined from the movement in the direction of the y-axis. In summary, in addition to the long time-scale motion of the jet ridge line presented before, and the jet component motion (fast and stationary), an additional motion on a shorter time-scale seems superimposed. The time-scale of this is of the order of a year.

3.2 Counter-jet

In 14 epochs (subset of the investigated data sets) between 1996.05 and 2011.65, we find evidence for jet components on the counter-jet side. The counter-jet component is at a distance of ∼0.70 mas and at a position angle of ∼49 deg in the time between 1996.05 and 2005.20. From 2005.20 till 2007.68 instead a component at a core distance of ∼ 0.15 mas and a position angle of ∼ 29 deg is observed. Between 2010.66 and 2011.65, we observe a counter-jet feature at ∼0.21 mas and ∼132 deg. After 2011.65, we find no evidence for counter-jet emission any more. A possible explanation for the appearance of the counter-jet features could be that a favourable viewing angle allows to see counter-jet emission. We do not have any further spectral information on these features on the counter-jet side. We mark the counter-jet components in Tables B1 with an **x**. We deliberately do not include the counter-jet components in the plots.

3.3 Time-scales based on the radio-jet motion

The radio jet reveals different types of movements. We here list the different time-scales derived from analysing in detail the kinematics of the radio jet.

(i) *Long time-scale motion* – The jet is moving in the plane of the sky. A possible explanation of this motion could be precession. The time-scale of the precession can be derived from comparing the times between similar locations of the jet in the sky. The last and most recent epoch of data analysed for this paper (2017.31) shows that the jet reached a similar position in the sky as in 1995.27 (Figs. 4a and b). We thus conclude that, based on the VLBA data alone, a full orbit of the precession has a time-scale of ∼22 yr. This time-scale compares quite nicely with twice the dominant periodicity time-scale quoted for the optical light-curve.

(ii) *Short time-scale motion* – The time-scale determined from motion of the stationary jet feature component **a** (see Fig. 5) is roughly 1 yr. The type of motion – upwards and downwards with regard to the position angle – could be consistent with rotation. The complete evolution of the position angle as function of time for component **a** is shown in Fig. 12. The ejection of jet features does not happen exactly with one component per year but in 13 yr of time (1994.1–2007.3) 12 jet components appeared in the jet. The ejection of components could be related to the jet rotation. Besides component **a**, two other jet components reveal stationary behaviour: **b** and **c**. These components appear at larger core separations and are less bright compared to **a**. Thus, fewer data points are available. For **a** 94 data points, for **b** 44, and for **c** 11 data points have been observed. **b** shows some indication for a similar behaviour as **a** – the position angle shows a roughly periodic increase and decrease on a time-scale which is of the order of ∼2 yr. This is larger than the ∼1 yr time-scale estimated for **a**. For **c** the data are not sufficient to check for this kind of motion.

Based on the analysis of the VLBA data, we find different motion scenarios in and of the OJ287-jet. These motions seem to be related to characteristic time-scales. In the following, we test whether these time-scales (of about 22 yr and 1 yr) are present in the radio light-curve (14.5 GHz) as well.

4 TIME SERIES ANALYSIS

Based on the method of creating Gaussian mock data[2] from any red noise power spectral density (PSD) (Timmer & Koenig 1995), and its modification to account for flux density distributions other than Gaussian (Witzel et al. 2012; Hora et al. 2014), we developed an approximate Bayesian computation (ABC) sampler for fitting the first order structure function of stochastic light curves (as defined in Hora et al. (2014), but here used in a logarithmic binning). This sampler enables us to determine the posterior distributions for the PSD parameters (slope and correlation time-scale) and the parameters of the flux-density distribution (Witzel et al. 2018). We assume the flux-density distribution at radio wavelengths to be lognormally distributed (with parameters μ, σ), and the measurement noise to be

[2]Mock data are the technical term for data simulated with some sort of random generator; in this case, a random generator that creates red noise light curves.

Table 1. The estimated times of ejection, proper motions, apparent speeds (based on linear regression), and the position angles of the jet components found and analysed in this manuscript are listed. In addition, we add further information on jet component motion from the literature. Three components (marked with **G**) were taken from Gabuzda et al. (1989) and Abraham (2000). Six components (marked with **T**) were derived from Tateyama et al. (1999). The apparent velocities of those values taken from the literature were recalculated using the cosmological parameters used in this paper.

Jet feature	Ejection time	Publication	μ (mas yr^{-1})	$\beta_{\rm app}$ (c)	η ($^\circ$)
a	–	this work	0.013 ± 0.001	0.191 ± 0.015	–
b	–	‘ ’	0.001 ± 0.002	0.015 ± 0.029	–
c	–	‘ ’	− 0.006 ± 0.002	− 0.088 ± 0.029	–
C1	1994.1	‘ ’	0.70 ± 0.05	10.30 ± 0.74	− 94.20 ± 0.19
C2	1994.8	‘ ’	0.68 ± 0.02	10.00 ± 0.29	− 92.70 ± 0.52
C3	1995.3	‘ ’	0.63 ± 0.02	9.26 ± 0.15	− 90.90 ± 0.25
C4	1995.5	‘ ’	0.58 ± 0.01	8.53 ± 0.15	− 90.30 ± 0.27
C5	1997.1	‘ ’	0.47 ± 0.01	6.91 ± 0.15	− 112.40 ± 1.06
C6	1997.9	‘ ’	0.46 ± 0.01	6.76 ± 0.15	− 111.80 ± 0.11
C7	1998.9	‘ ’	0.46 ± 0.01	6.76 ± 0.15	− 114.00 ± 0.53
C8	2000.1	‘ ’	0.45 ± 0.01	6.62 ± 0.15	− 124.70 ± 0.32
C9	2000.8	‘ ’	0.39 ± 0.01	5.73 ± 0.15	− 121.70 ± 0.36
C10	2002.5	‘ ’	0.43 ± 0.01	6.32 ± 0.15	− 121.20 ± 0.40
C11	2002.9	‘ ’	0.32 ± 0.01	4.70 ± 0.15	− 125.90 ± 0.17
C12	2007.3	‘ ’	0.34 ± 0.02	5.00 ± 0.29	− 136.40 ± 0.12
G1	1969.5	Gabuzda et al. (1989)	0.27 ± 0.04	4.0 ± 0.6	− 100.0 ± 10.0
G2	1978.7	Gabuzda et al. (1989)	0.25 ± 0.04	3.7 ± 0.6	− 120.0 ± 10.0
G3	1983.3	Gabuzda et al. (1989)	0.31 ± 0.04	4.6 ± 0.6	− 150.0 ± 10.0
T1	1990.8	Tateyama et al. (1999)	0.74 ± 0.40	10.88 ± 6.0	− 109.0 ± 10.0
T2	1992.6	Tateyama et al. (1999)	0.44 ± 0.05	6.5 ± 0.7	− 110.0 ± 10.0
T3	1992.6	Tateyama et al. (1999)	0.52 ± 0.09	7.6 ± 1.3	− 98.0 ± 10.0
T4	1993.5	Tateyama et al. (1999)	0.40 ± 0.13	5.88 ± 1.9	− 89.0 ± 10.0
T5	1994.7	Tateyama et al. (1999)	0.46 ± 0.05	6.762 ± 0.735	− 88.0 ± 10.0
T6	1995.8	Tateyama et al. (1999)	0.58 ± 0.07	8.526 ± 1.029	− 86.0 ± 10.0

Gaussian and white.[3] For 14.5 GHz, we find the parameter posterior distributions presented in Fig. 7. While not all parameters are well constrained (e.g. the flux density distribution is strongly affected by the temporal correlations that dominate the data for an observation length of only a couple of times longer than the coherence time-scale), these distributions represent the most general set of red noise light curves that show similar temporal properties as the observed data. However, these light curves are purely stochastic, i.e. they don’t incorporate any deterministic components.

Based on these distributions we draw 10 000 random red noise light curves. We compute the Lomb-Scargle periodograms of the observed data and the random light curves [following the description in VanderPlas (2018)], from which at each frequency we calculate the mean, the 95 per cent, and the 99.7 per cent quantiles. The resulting periodograms for the time-scale range of interest are shown in Figs 8 and 9. Additionally to the normal periodogram that is based on sines, we use so called multiterm periodograms that allow for more complex shapes of periodic signals.

The periodograms do not show very clear evidence for period at any time-scale. Thus, for 4.8 and 8 GHz we cannot prove a periodicity in a mathematical strict sense. For this paper, we would like to concentrate on the yearly time-scale. While all three radio light curves show some indication of possible excess power, the 14.5 GHz data is most promising to allow a successful detection and quantification. We also investigated the periodograms of the optical data and the 4.8 and 8 Ghz radio light curves. While all three radio light curves show some indication of possible excess power, the 14.5 Ghz data around the yearly time-scales seems most promising to allow us a successful detection and quantification of a periodic signal. In contrast, the optical data does not show much indication of excess power. Even the much discussed 12 yr optical cycle is not visible (and thus not a strict periodicity). Therefore for the sake of brevity, we concentrate on the analysis of the 14.5 GHz data in the range of 100 to 1000 d.

We find four significant peaks around a period of 1 yr. However, the significance at a given frequency is not sufficient to claim a detection because our periodograms have several thousand frequency bins. This makes the occasional occurrence of 3σ peaks probable. For white noise, a false alarm probability can be calculated based on the number of effective frequencies, i.e. the number of statistically independent frequencies. The number of effective frequencies can simply be calculated from the frequency range divided by the typical peak width in the periodogram (which itself is proportional to the length of the light curve). However, for red noise the PSD is correlated over a wide range of frequencies, and it is not clear how to determine the number of effective frequencies.

Based on our red noise model from the Bayesian analysis above, we used a Monte Carlo method to estimate a false alarm probability for our case. The pattern of four consecutive significant peaks indicate the possibility of a real periodicity that leaked power to a number of surrounding frequencies. To test this hypothesis, we analyse how often four adjacent significant peaks can be found in a frequency range of 5.3×10^{-4} d s^{-1}. We find a similar pattern in 15 of the 10000 simulated light curves, which constitutes an upper limit for the false alarm probability of 1.5×10^{-3} (better than 3σ). This entire method is designed for addressing the problems for the window function and the effects of unequal sampling in the context of Lomb–Scargle periodograms. The significance analysis is based on

[3]The priors for the lognormal (2), PSD (2), and white noise (1) parameters are: a: uniform on [0.1, 4.5]; b: uniform in frequency on [10^{-6}, 10^{-3}]; noise: Gaussian with $\mu_{\rm noise} = 0.3$ Jy, $\sigma_{\rm noise} = 0.05$ Jy; lognormal parameters μ uniform on [0.1,10.0];and σ uniform on [0.01, 5.0].

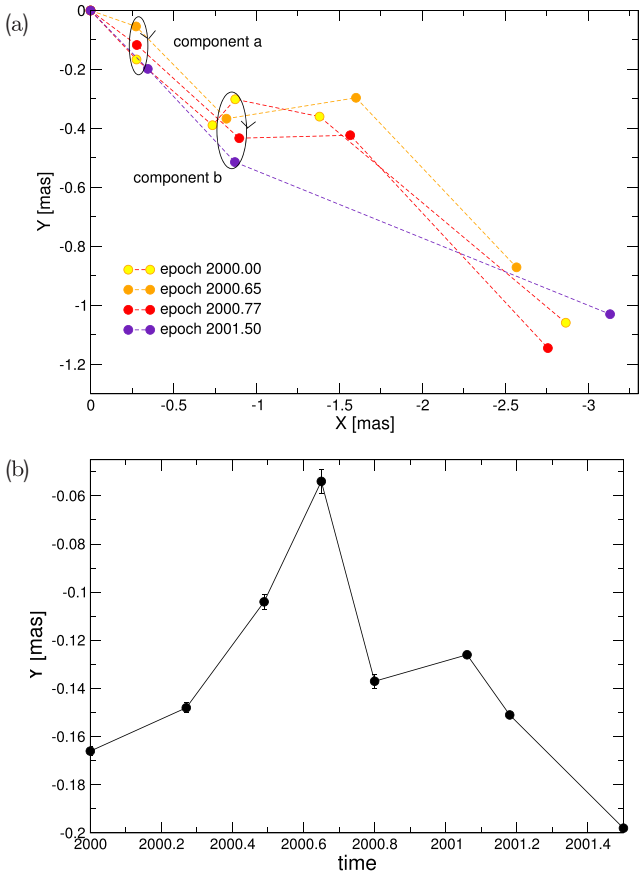

Figure 5. Component motion for the time between the two prominent flares visible at 2000.0 and 2001.5 (a). Four epochs within the time span (2000.0–2001.5) were selected for display. Close inspection of component **a** reveals evidence for a rotation (circle indicates motion of component **a**). We also indicate the rotational motion for component **b** by a circle and a black arrow indicating the sense of rotation. The position angle for component **a** in the same time span increases up to a maximum value and then decreases again, shown in (b). All values for all epochs between 2000.0 and 2001.5 are shown in (b).

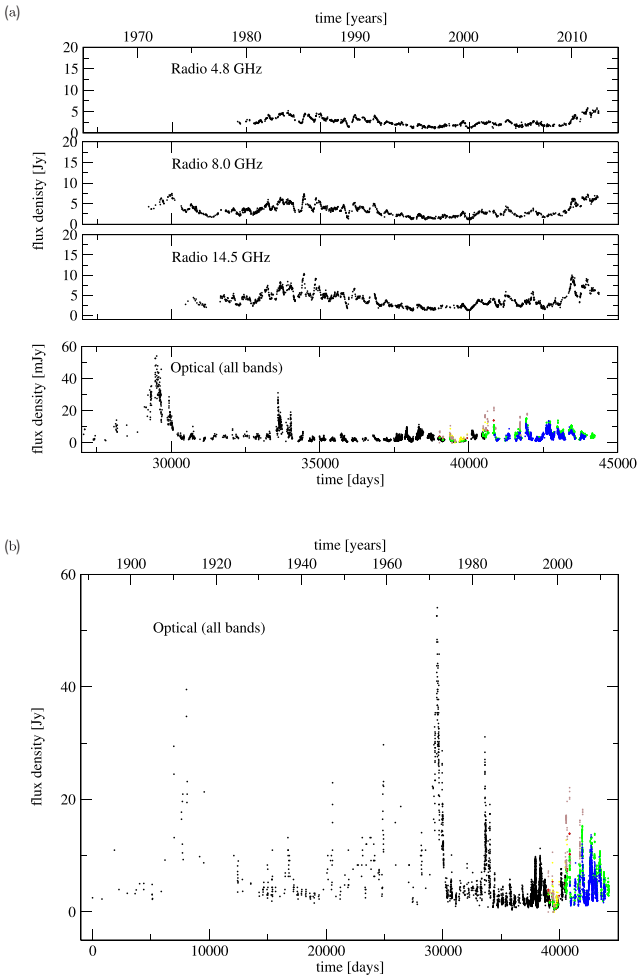

Figure 6. (a) Radio (UMRAO) and optical light curves including historical and recent data sets. The colours in the optical light curve in (a) and (b) refer to the same bands. (b) The optical light curve is compiled from historic *V*-band data (black), historic *R*-band data (blue), and new data obtained by the Abastumani telescope in *R* band (green), *I* band (yellow), *V* band (red), and *B* band (brown). The origin of the time axis is the first measurement of the historical optical light curve (2411753.00 JD).

red noise mock data on the same time support. This means that the method applied is dealing with all effects of the window function of the observed data and its interaction with correlations in red noise. Therefore, the detected periodicity cannot be simply explained by artefacts of the window function. For illustration, we show the light curve folded with the period of 378 d in the left-hand panel of Fig. 9 (the maximum of the array of significant periodogram peaks). We fold all the data into one phase and randomly distribute two-thirds of the points over low additional phases. Then we re-bin the data with bins of 0.1 phases. This averaging is eliminating a good fraction of the red noise power in the data.

While these findings make it probable that the radio data indeed is composed of a random red noise component (with a PSD slope of a $\approx$2 and an indication of a correlation time-scale of $b \gtrsim 2200$ d) and a deterministic signal, it does not help to determine its precise frequency or shape. The situation is aggravated by two facts: the proximity of a periodicity caused by the yearly observing campaigns that we demonstrate in Fig. 9, and the fact that spectral leakage patterns are influenced in their amplitude and location of peak frequencies by the underlying red noise. A precise analysis of the shape and frequencies of the deterministic signal will be published independently. For this work, we conclude that there is marginal significance for a periodic signal at time-scales between 340 and 440 d.

The published cycles and periodicities derived from light curves vary by a large margin. While convincing evidence for the cycle of 11–12 yr has been presented for the optical data, the value for the period at the yearly time-scale is comparatively uncertain ranging between 1.12 and 1.8 yr (Hughes et al. 1998; Hovatta et al. 2008; Donskykh 2016). Potential detections of periods at 1.6–4.0 and 6–10 yr were also reported. We also analysed the optical data and the other two radio frequencies, and in the following, we summarize our findings without presenting details. We find indication of excess power at yearly time-scales at 8.0 and 4.8 GHz, but it is not as significant as in the case of the 14.5 GHz. Other periodicities do not reach the necessary level of confidence, except for periods of one day in all radio light curves and some additional peaks at a few days in the 4.8 GHz, all of which again can be explained by the data cadence. No significance could be established for periods in the 2–10 yr range. The optical data do not show any significant

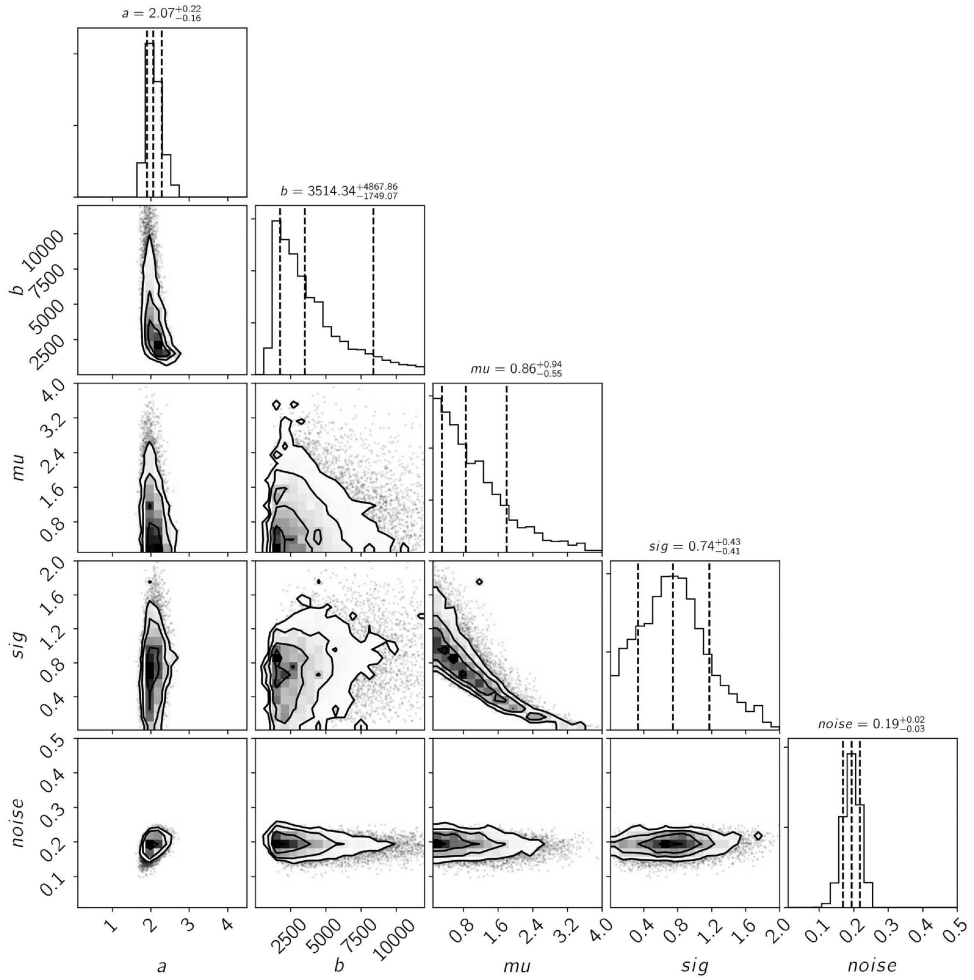

Figure 7. Corner plot of the ABC structure function fit. The parameters are the slope (a1) and break frequency (b1) of the PSD, the lognormal parameters μ and σ, and the white measurement noise. The measurements noise and the PSD slope are well constrained, while the break time-scale is indicated to be $\gtrsim$2200 d. The lognormal parameters are not well determined due to the fact that the length of the data set is not much longer than the break time-scale. However, sampling from these parameter distributions and creating random light curves for each of the drawn parameter sets results in the most general sample of light curves against which significance in the Lomb–Scargle analysis can be established.

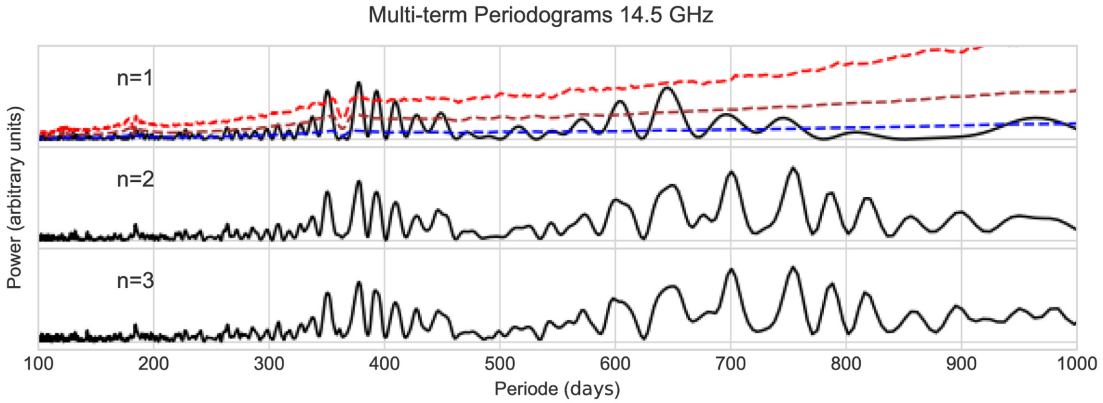

Figure 8. Lomb–Scargle periodogram of the 14.5 GHz light curve in the range of periods from 100 to 1000 d. The three panels show three different orders of multiterm periodograms (with $n = 1$ a pure sine). For $n = 1$, we derived for each frequency the average value (blue), the 95 per cent quantile (brown), and the 99.7 per cent quantile (3σ, red) from pure red noise light curves that fit the structure function of the observed data. Two groups of distinct peaks are noticeable, both related to a deterministic signal in the range of 340−440 d present in the data: the first group is caused by spectral leakage and shows four significant peaks, the second group is most likely the first higher harmonic and does not reach the 99.7 per cent significance level. The units of the y-axis are arbitrary.

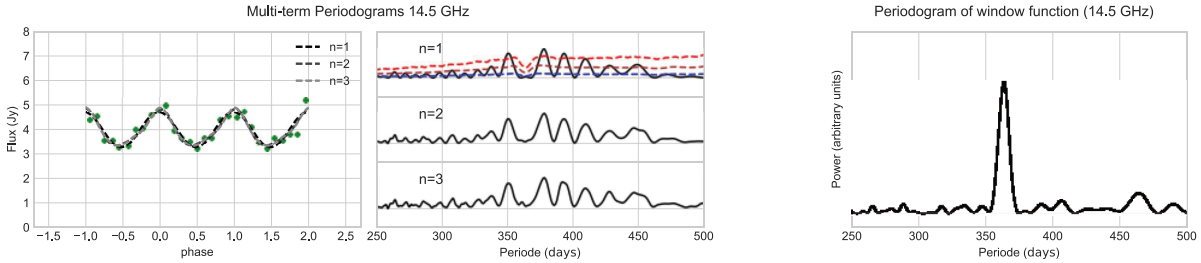

Figure 9. Left two plots: Close-up of the periodogram presented in Fig. 8 between 250 and 500 d and data folded on to three phases at a period of 378 d (the highest peak of the group of peaks related to the period of 366 d). The data show a clear sinusoidal variation. At the position of ∼365 d, both the real data and the confidence levels show a minimum cause by interaction with the window function. Right: Periodogram of the window function (computed from a light curve with the same time support as the real data, but with constant flux of one for all times). A clear peak due to the yearly observing campaigns is visible at 363 d. The units of the *y*-axis are arbitrary.

power beyond what can be expected due to red noise. However, we find in our tests that the extremely bright outbursts and their double-peak pattern at the approximate rate of once per 11–12 yr show a dramatically different distribution of flux densities than the rest of the optical data, and cannot be described with the same red noise process. This fact alone justifies to think of these bright outbursts as distinct events, and while not strictly periodic, they establish the published cycle of 11–12 yr convincingly. It is interesting to note that the coherence time-scale of the underlying red noise at 14.5 GHz is of the same order (about a decade) as the cycle in the optical data.

5 MODELLING THE JET PRECESSION

In the following, we study whether the changes in the position as well as the apparent velocities of the jet components may be explained by jet precession. The kinematic model is based on the fact that the jet at a given time consists of more components ejected at time t_0 with the velocity β in units of c in the comoving frame. Then the apparent velocity $\beta_{\rm app}$ in units of c in the observer's frame is given by

$$\beta_{\rm app} = \frac{\beta \sin \Phi(t)}{1 - \beta \cos \Phi(t)}, \tag{1}$$

where β is related to the Lorentz factor γ by $\gamma = 1/\sqrt{1-\beta^2}$ and $\Phi(t)$ is the angle between the direction of the motion of the component and the line of sight. The angle Φ and the position angle η of the jet components can be expressed as functions of the xy coordinates on the sky e.g. Abraham (2000),

$$\Phi(t) = \arcsin\left(\sqrt{x(t)^2 + y(t)^2}\right),$$
$$\eta(t) = \arctan\left(\frac{y(t)}{x(t)}\right), \tag{2}$$

with Cartesian coordinates in the observer's frame,

$$x(t) = A(t)\cos\eta_0 - B(t)\sin\eta_0,$$
$$y(t) = A(t)\sin\eta_0 + B(t)\cos\eta_0, \tag{3}$$

and with

$$A(t) = \cos\Omega\sin\Phi_0 + \sin\Omega\cos\phi_0\sin\omega(t-t_0),$$
$$B(t) = \sin\Omega\cos\omega(t-t_0), \tag{4}$$

where Ω is the half-opening angle of the precession cone, Φ_0 is the angle between the precession cone axis and the line of sight, and η_0 is the projected angle of the cone axis in the plane of the sky. The geometry of the model is schematically shown in Fig. 11. The precession angular velocity $\omega = 2\pi/P$ and the reference time t_0 are searched for in the fitting procedure as well as the Lorentz factor γ, and the angles Ω, Φ_0, and η_0.

Table 2. Best fit parameters and the associated uncertainties calculated from the covariance matrix.

Quantity	Value
t_0	(1998.9 ± 0.8) yr
P	(24 ± 2) yr
γ	10 ± 1
Ω	$(10 \pm 3)^\circ$
ϕ_0	$(12 \pm 3)^\circ$
η_0	$(-149 \pm 40)^\circ$

We calculated the viewing angle values by assuming that the jet has the minimum Lorentz factor required to achieve the observed apparent velocity of the component. The viewing angle values are not fitted but calculated under the afore-mentioned assumption. We think it is reasonable to assume that intrinsically the jet velocity should not change. However, the apparent velocity appears different because of the viewing angle changes which we argue might be caused by precession. In principal, the apparent Lorentz factor is naturally affected by the viewing angle that may change depending on the physics operating the jet, e.g. such as precession, or jet bending, etc. The intrinsic jet velocity may change over longer spatial scales (e.g. kpc) due to environmental effects (external gas pressure, gravity, accompanied by a change in opening angle). However, here we consider the jet motion on shorter distances. Note, that what we see is a pattern speed in the radiation map and not the underlying kinematic motion of the emitting material. The fit of the precession model to the data is done simultaneously for ($\beta_{\rm app}$, t) and (η, t) data sets using the global least-square fitting. We consider the components listed in Table1 along with their parameters. The results of the simultaneous fit are presented in Table 2. In Fig 10, we plot the best fit precession model from Table 2 and the data from Table 1. We discuss the interpretation of the data in the forthcoming sections.

5.1 Modelling the combined jet precession and nutation

Visually inspecting the change of the position angle for component **a**, a hint of extra motion on top of the jet precession can be seen. We hypothesize that component **a** rotates in the jet frame. For simplicity,

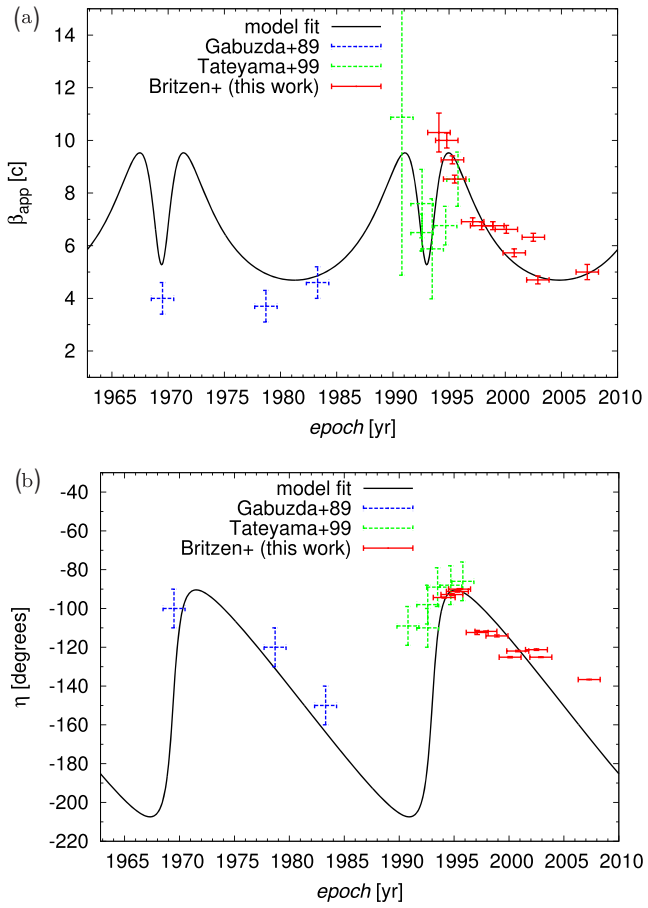

Figure 10. (a) Best-fitting precession model for the apparent velocities $\beta_{\rm app}$ of the observed components. (b) Best-fitting precession model for the position angle η of the fast components. We performed simultaneous least-square fitting for both $\beta_{\rm app}$ and η based on the results presented in Table 2.

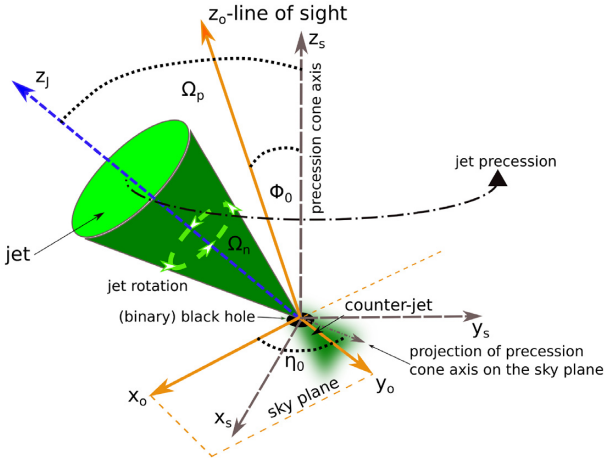

Figure 11. Scheme of the model for precession and rotation of OJ287. Three reference frames are shown: the jet frame, the source frame, and the observer frame. Half-opening angles of the precession cone $\Omega_{\rm p}$ and of the jet rotation $\Omega_{\rm n}$ are depicted. In the observer frame, the precession cone axis is described by the angles Φ_0 and η_0.

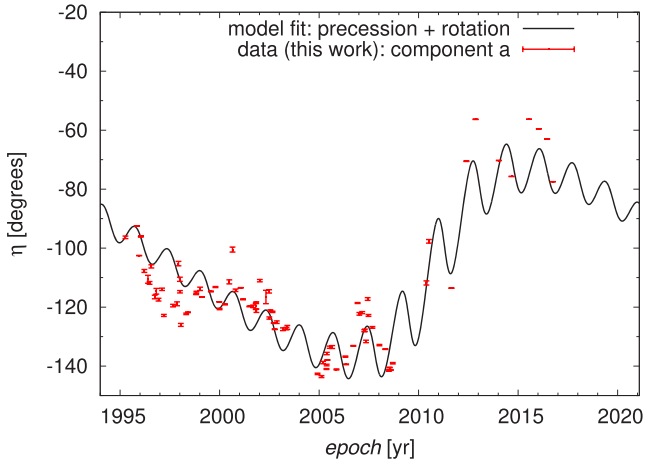

Figure 12. The fit of the combined precession and nutation model to the position angles (with error bars) of the most prominent stationary component **a** as a function of time.

Table 3. Quantities used in the precession-nutation model of the jet.

Notation	Definition
$P_{\rm p}$	Precession period
$P_{\rm n}$	Nutation period
$\Omega_{\rm p}$	Half-opening angle of the precession cone
$\Omega_{\rm n}$	Half-opening angle of the jet
Φ_0	Angle between the precession cone axis and the line of sight
η_0	Projected angle of the cone axis in the plane of the sky
t_0	Reference time

we assume that component **a** rotates around the jet axis in a uniform circular way, i.e. in a similar way as the Earth's axis precession and nutation model. The intrinsic kinematics might be more complex; however, the nutation model will give a basic idea of the associated periods and the overall geometry of such a composite motion.

In the following relations, we use the notation as defined in Table 3.

In the frame of the jet, nutation with the angular velocity $\omega_{\rm n} = 2\pi/P_{\rm n}$ of a stationary component with the vector components $\boldsymbol{n}_{\rm J} = (x_{\rm J}, y_{\rm J}, z_{\rm J})$ can be expressed as

$$x_{\rm J} = \sin\Omega_{\rm n} \sin\left[\omega_{\rm n}(t - t_0)\right], \tag{5}$$

$$y_{\rm J} = \sin\Omega_{\rm n} \cos\left[\omega_{\rm n}(t - t_0)\right],$$
$$z_{\rm J} = \cos\Omega_{\rm n}. \tag{6}$$

To transform this motion to the observer's frame, a series of rotations is needed. Let us denote a general rotation matrix $\boldsymbol{R}_{\rm o}(\alpha)$ around axis o by angle α. The vector components $\mathbf{n}_{\rm s}$ in the source frame can be calculated using the following equations:

$$\boldsymbol{n}_{\rm s} = \boldsymbol{R}_z(\omega_{\rm p}(t - t_0))\boldsymbol{R}_y(\Omega_{\rm p})\boldsymbol{n}_{\rm J}, \tag{7}$$

where $\omega_{\rm p}= 2\pi/P_{\rm p}$. Two more rotations are required to obtain the components of the nutation vector $\boldsymbol{n}_{\rm o}$ in the observer's frame,

$$\boldsymbol{n}_{\rm o} = \boldsymbol{R}_z(\eta_0)\boldsymbol{R}_y(\Phi_0)\boldsymbol{n}_{\rm s}. \tag{8}$$

The geometry of the combined precession-nutation model of the jet is shown in Fig. 11. We fit equations (8) to the temporal evolution of the position angle η of component **a**. The fit of the model, which

Table 4. Best-fitting values for the precession-nutation model.

Quantity	Best-fitting value
t_0	(1997.4 ± 0.6) yr
P_p	(27 ± 5) yr
P_n	(1.6 ± 0.1) yr
η_0	$-105^\circ \pm 8^\circ$

includes intrinsically both the precession of the jet and its nutation, is plotted in Fig. 12 along with the data for component **a**. The least-square fitting converges with the parameters listed in Table 4. The half-opening angles Ω_p, Ω_n, and the angle Φ_0 are not well-constrained from the fit. This may be due to the fact that we are only fitting the position angles of one component, not including the apparent velocities or more components. Within uncertainties, the ratio of half-opening angles $\Omega_p/\Omega_n \approx 4$ implies the jet half-opening angle of $\Omega_n \sim 4.5^\circ$ when taking into account the previous simultaneous fit for $\eta(t)$ and $\beta_{app}(t)$ with the best-fitting value for $\Omega_p = (10 \pm 3)^\circ$.

The best-fitting periods $P_p = (27 \pm 5)$ yr and $P_n = (1.6 \pm 0.1)$ yr obtained from the precession-nutation fit are consistent within uncertainties with the independent periodicity search, which had only very general assumptions.

In short, the model fit and the periodicity analysis both provide a strong case for the longer period of ∼20 yr, which is best explained by the precession of the whole jet, and the shorter period of ∼1 yr, which seems to be associated with the motion on the top of the precession motion – possibly a nutation-like motion of the jet.

5.1.1 Nutation might cause jet rotation – Comparison to SS433

As we have shown above, the data can nicely be explained by a combination of precession and nutation, assuming that what we observe is not the rotating jet material but the rotating jet-axis which rotates on the nutation cone superimposed on the precession motion. This has been observed and modelled in the case of the X-ray binary SS433: in addition to jet precession (caused by the disc) an additional nutation of the jet has been found. This nutation occurs with a period of 6.5 d and can be linked to the orbital period of the binary (13 d) (Monceau-Baroux et al. 2014). In the case of OJ287, a similar effect is possible and could explain the motion on top of the precession. Comparing the time-scales for precession in SS433 (162 d) with the time-scale for precession in OJ287 (22 yr), the ratio (50) is of the same order as for the ratio (56) of the time-scales for the nutation/rotation (6.5d/1 yr) in SS433 and OJ287. We thus propose that a similar mechanism is at work in both systems, although SS433 is a stellar binary object and OJ287 an SMBBH. As shown in Fig. 11 and discussed in Section 5.1, our data are consistent with a model of precession plus nutation.

5.2 Optical and radio variability due to Doppler boosting

The precession model for OJ287 was applied by Abraham (2000) to explain the optical outbursts by Doppler boosting of optically thin optical emission when the jet approaches the line of sight and the beaming factor is increased. They derived the geometrical parameters of the precessing jet based on the kinematics of superluminal features in the pc-scale radio jet. The kinematic parameters were obtained from VLBI measurements at 6 and 3.6 cm (Roberts, Gabuzda & Wardle 1987; Gabuzda, Wardle & Roberts 1989; Gabuzda & Cawthorne 1996). In addition, they also confine the Lorentz factor of the bulk motion of the jet, $\gamma \approx 7$. The Doppler factor is defined as $\delta(\Phi, \gamma) = \gamma^{-1}\{1 - \beta\cos[\Phi(t')]\}^{-1}$. Looking at Fig. 6, we are tempted to suggest that a series of radio maxima appears on a time-scale of ∼24 yr, which may be associated with the precession period (24 ± 2 yr, see Section 5). The measured flux density $S_\nu \propto \delta^{p+\alpha}$, where δ is the Doppler factor, $p = 2$ for a continuous jet and α is the spectral index, $S_\nu \propto \nu^{-\alpha}$ (Abraham 2000). The spectral index based on the radio measurements between 4.8 GHz and 14.5 GHz is variable, but ranges from flat to inverted, $\alpha \in (0, -1)$. The ratio of maximum and minimum flux densities in Fig. 6 is approximately 5, which gives the range of the ratio of maximum and minimum Doppler-boosting factors ≈2.2 for $\alpha = 0$ and the ratio of Doppler factors $\delta = 5$ for $\alpha = -1$. We show in Fig. 13 the variability of the Doppler factor. The radio variability could thus be explained solely by a precessing optically thick jet emission, in case the spectral break is at $\nu > 14.5$ GHz. In addition, we superimpose the radio light curve obtained at 14.5 GHz in Fig. 13 and show that the basic shape can be produced by variable Doppler boosting.

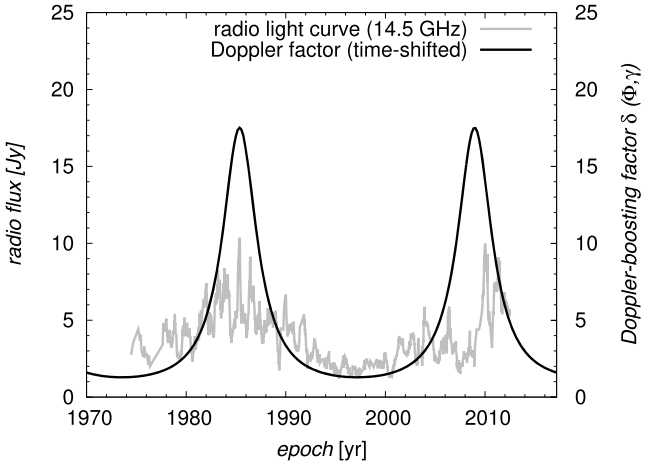

Figure 13. The Doppler factor Delta (solid black line) varies between the minimum value of $\delta_{min} = 1.3$ and the maximum value of $\delta_{max} = 17.5$. Overplotted (grey line) is the flux-density light curve at 14.5 GHz. The Doppler factor has been shifted in time by 7.65 yr to match the peaks of the radio light curve. The reference time t_0 thus differs from the values listed for t_0 in Tables 2 and 4.

5.2.1 Constraints on the Lorentz factor

Taking $\beta_{app,\,max} = 10.30 \pm 0.74$ (from Table 1, **C1**), the minimum Lorentz factor is given by $\gamma_{min} = \sqrt{\beta^2_{app,max} + 1} \approx 10.35$, which is also used for calculating the Doppler factor δ for the viewing angle $\sin\Phi = 1/\gamma \rightarrow \Phi \sim 5.5^\circ$. The Doppler factor causes the flux enhancement in the observer frame according to $S = \delta^{p+\alpha} S'$, where $p = 2$ for a continuous jet and $p = 3$ for discrete sources. For the jet emission with the power-law index of $\alpha \sim -1$, we would thus expect the flux density enhancement of the order of 10. The optical as well as radio variability may be explained by the variable boosting of the non-thermal emission of an underlying pc-scale jet since the Doppler factor varies with precession (Caproni & Abraham 2004b):

$$S(\nu) = S'(\nu)\delta(\Phi, \gamma)^{p+\alpha} \quad (9)$$

with Doppler factor $\delta(\Phi, \gamma)$ and $S'(\nu)$ as the flux density emitted in the comoving frame. For an optically thin case, $S_\nu \propto \nu^{-\alpha}$, the

spectral index α is positive and the parameter p is set to 2 for a continuous jet and to 3 for discrete features. Valtonen & Pihajoki (2013) already propose that the quasi-periodic nature of the optical light curve arises from a helical jet being observed from a small and varying viewing angle.

6 ORIGIN OF THE JET PRECESSION

The precession of the jet may be explained by several schemes. In Seyfert galaxies, it was proposed that the pericentre advance of an elliptical accretion disc is responsible for the precession (Eracleous et al. 1995), or the precession of a single spiral arm in a circular disc (Storchi-Bergmann et al. 2003). It was also proposed that the precession may be caused by the radiation-induced warp in the disc (Pringle 1996; Storchi-Bergmann et al. 1997). The precession of the jet may be explained by several plausible set-ups, two of which are illustrated in Fig. 11 and discussed in the following text.

6.1 Lense-Thirring precession of the BH

The angular momentum of a single rotating (Kerr) BH and that of an accretion disc (given the jet direction) are misaligned (Caproni, Mosquera Cuesta & Abraham 2004), which would be expected for the final BH resulting from a galaxy merger, for which there is some evidence in case of OJ287 based on the offset between the OJ287 host and the AGN (Yanny, Jannuzi & Impey 1997). The misalignment might lead to Lense-Thirring precession of the BH. The subject of Lense-Thirring frequencies has been applied extensively to explain quasi-periodic oscillations in BH binaries (e.g. Stella & Vietri 1998; Stella & Possenti 2009). The inner part of the disc as well as the BH can be driven to precess by the outer part of the disc if it has a sufficient angular momentum. Lu (1992) derived a formula for the precession period of the BH $P_{\rm LT}$ as a function of the rotation parameter $a_\bullet$, the viscosity parameter $\alpha_{\rm vis}$, the BH mass $M_\bullet$, and the accretion rate $\dot{M}_\bullet$,

$$P_{\rm LT} = 2\pi/\Omega_{\rm LT} = 10^{9.25} a_\bullet^{5/7} \alpha_{\rm vis}^{48/35} \left(\frac{M_\bullet}{10^8\,{\rm M}_\odot}\right)^{1/7} \left(\frac{\dot{M}_\bullet}{10^{-2}\,{\rm M}_\odot\,{\rm yr}^{-1}}\right)^{-6/5} {\rm yr} \quad (10)$$

which for the Kerr angular momentum parameter $a_\bullet = 0.1$ and the viscosity parameter $\alpha_{\rm vis} = 0.1$ leads to $P_{\rm LT} = 1.7 \times 10^7$ yr for $M_\bullet = 4 \times 10^8\,{\rm M}_\odot$ and $P_{\rm LT} = 3.1 \times 10^7$ yr for $M_\bullet = 1.8 \times 10^{10}\,{\rm M}_\odot$. The viscosity parameter has been derived based on observational studies (King, Pringle & Livio 2007). In general, the dependency on the BH mass is weak, so in order to have the precession period of the order of $P_{\rm LT} = 10$ yr, the rotational parameter would have to be very small, $a_\bullet \approx 10^{-9}$. The scenario of the BH precession is thus rather implausible. Instead, we focus further on the more relevant case of an accretion disc precession.

6.2 Lense-Thirring precession of the accretion disc

The amplitude of the precession angular velocity $\omega_{\rm LT}$ decreases with the cube of the distance and becomes negligible at larger distances. In general, the precession period of the disc/jet, under the assumption of a rigid precession, depends on the BH's angular momentum $J_{\rm BH} = G M_{\rm BH}^2 |a_\bullet|/c$, with $-1 \le a_\bullet \le 1$, with the minus sign for the retrograde rotation. Another parameter is the extent of the precessing part of an accretion disc, from the inner radius $R_{\rm in} = \xi_{\rm in} R_{\rm g}$ up to the outer part $R_{\rm out} = \xi_{\rm out} R_{\rm g}$, where $R_{\rm g} = GM_\bullet/c^2 = 5.9 \times 10^{13} (M_\bullet/4 \times 10^8\,{\rm M}_\odot)\,{\rm cm} = 0.019 (M_\bullet/4 \times 10^8\,{\rm M}_\odot)\,{\rm Mpc}$ is the gravitational radius. We may associate the inner radius of the accretion disc with the marginally stable orbit of a Kerr BH $R_{\rm ms} = \xi_{\rm ms} R_{\rm g}$, where $\xi_{\rm ms} = 3 + A_2 \mp [(3 - A_1)(3 + A_1 + 2A_2)]^{1/2}$, with $A_1 = 1 + (1 - a_\bullet^2)^{1/3}[(1 + a_\bullet)^{1/3} + (1 - a_\bullet)^{1/3}]$ and $A_2 = (3a_\bullet^2 + A_1^2)^{1/2}$ (Caproni et al. 2004). For the maximum prograde rotation, we get $\xi_{\rm ms} = 1$, while for the maximum retrograde rotation $\xi_{\rm ms} = 9$. The disc precession also depends on the density profile of the disc. Assuming that the disc surface density depends only on the radius, we may write $\Sigma_{\rm d} = \Sigma_0 \xi^s$, where we take $s \in \{-2, -1, 0\}$, i.e. decreasing or constant surface density with the distance from the BH. Finally, the disc precession may be obtained by the following relation (Caproni et al. 2004),

$$P_{\rm prec} = \frac{2\pi G M_\bullet}{c^3} \frac{\int_{\xi_{\rm ms}}^{\xi_{\rm out}} \Sigma_{\rm d}(\xi)[\Upsilon(\xi)]^{-1} \xi^3 {\rm d}\xi}{\int_{\xi_{\rm ms}}^{\xi_{\rm out}} \Sigma_{\rm d}(\xi)\Psi(\xi)[\Upsilon(\xi)]^{-2} \xi^3 {\rm d}\xi}, \quad (11)$$

where $\Upsilon(\xi) = \xi^{3/2} + a_\bullet$ and $\Psi(\xi) = 1 - (1 - 4a_\bullet \xi^{-3/2} + 3a_\bullet^2 \xi^{-2})^{1/2}$. We apply equation (11) and consider a BH mass of $M_\bullet = 4 \times 10^8\,{\rm M}_\odot$ and the outer radius of the precessing part of the disc $R_{\rm out} = 100\,R_{\rm ms}$ and $R_{\rm out} = 1000\,R_{\rm ms}$. The precession period $P_{\rm prec}$ in years is plotted in Fig. 14 as a function of the spin parameter $a_\bullet$. The horizontal line represents the precession period for OJ287 $P_{\rm prec}^{\rm obs} = 24$ yr, which corresponds to $P_{\rm prec} = 18.4$ yr. According to the precession period in Fig. 14, the precession for OJ287 can be reproduced for a slowly rotating BH ($a_\bullet = 0.1$ and $a_\bullet = -0.12$ in both a prograde and retrograde way for a smaller disc and $a_\bullet = 0.24$, $a_\bullet = -0.6$ for a larger disc) and a steep density profile ($s = -2$). For the shallower profile ($s = -1$), the precession period of OJ287 can be matched only for a smaller disc (left-hand panel) for a larger prograde spin, $a_\bullet = 0.65$. This value depends on parameters as the disc surface density profile, the outer disc radius, and the BH mass. The disc profile and the outer disc radius of the precessing part of the disc are difficult to determine. Because we have no constraints on the BH spin (free parameter), we plot the Lense-Thirring precession for the full range $-1 \le a_\bullet \le 1$. The disc surface density profile is a free parameter as well and we thus plot the dependences of the Lense-Thirring precession on the BH spin for three different power-law profiles of the disc surface density (s = −2, −1, 0). The same applies for the disc outer radius. We follow the analysis of the Lense-Thirring precession period by Caproni et al. (2004; their equation 3). The authors investigate the dependence of the Lense-Thirring precession period on the disc profile in more detail. We can neither confine the disc surface density profile nor the BH spin at the moment, but we show that the mechanism of the Lense-Thirring precession provides realistic parameters in the case of OJ287. Thus, the observed precession could be caused by Lense-Thirring precession of the disc of a single BH. Comparing our derived value with the measured precession periods listed by Caproni et al. (2004; their table 1),all the values are found in a range between 0.29 and 22 yr.

6.3 Precession due to the torques exerted by a binary BH model companion

The jet may precess due to the torques arising by the misalignment of an accretion disc and the orbital plane of a binary BH (Katz 1997). Katz (1997) already proposed that the optical flaring of OJ287 within a period of about 12 yr is caused by the motion of a precessing relativistic beam across our line of sight. In addition, the author explained the precession by a torque of an accretion disc due to a companion object. Such a configuration can indeed lead to the periods of the order of several years (Caproni & Abraham 2004a).

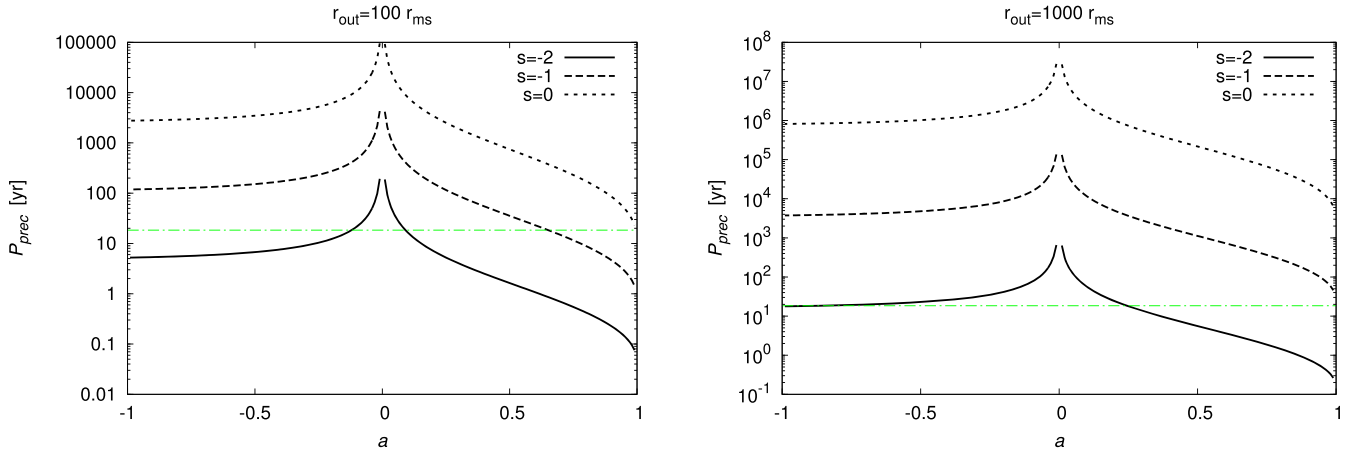

Figure 14. The precession period for OJ287 as a function of the spin parameter. In the panel on the left, the outer radius of the disc is taken to be $R_{\rm out} = 100\,R_{\rm ms}$. Different lines correspond to the different power-law slopes of the disc surface density according to the legend. The panel on the right shows the same as the left-hand panel, but for the outer radius of the disc $R_{\rm out} = 1000\,R_{\rm ms}$. In both left-hand and right-hand panels, the green horizontal line marks the assumed period of precession of approximately 18.4 yr in the comoving frame of the source.

Let us consider the components of the binary with the masses of $M_{\rm p}$ for the primary BH and $M_{\rm s}$ for the secondary BH with the total mass of $M_{\rm tot} = M_{\rm p} + M_{\rm s}$. The orbital period of the binary $P_{\rm ps}$ and the distance of the components $r_{\rm ps}$ are mutually connected via the Kepler law

$$r_{\rm ps}^3 = \frac{G M_{\rm tot}}{4\pi^2} P_{\rm ps}^2. \quad (12)$$

The observed period $P_{\rm ps}^{\rm obs}$ and the period in the comoving frame $P_{\rm ps}$ are related as

$$P_{\rm ps} = \frac{P_{\rm ps}^{\rm obs}}{1+z}. \quad (13)$$

For the total mass of the binary, we consider the value derived from the BH–bulge correlations ($M_\bullet$–σ and $M_\bullet$–$L_{\rm bulge}$) $M_{\rm tot} = 4 \times 10^8\,{\rm M}_\odot$ (Liu & Wu 2002), which is probably a more realistic value than the model mass described by Valtonen et al. (2016), where the primary BH with the mass $M_{\rm p} = 1.8 \times 10^{10}\,{\rm M}_\odot$ hits an upper limit for the maximum observable mass of the SMBBH, which is estimated to be $M_{\rm max} \approx 5 \times 10^{10}\,{\rm M}_\odot$ (King 2016; Eckart et al. 2017). The observed precession period is estimated from the variability indicated in Fig. 6, $P_{\rm bin}^{\rm obs} \approx 24$ yr, which is $P_{\rm prec} = 24/(1 + 0.306)\,{\rm yr} = 18.4\,{\rm yr}$ in the comoving frame. We may associate this period with the jet and disc precession of the system $P_{\rm jet} = P_{\rm disc} \approx P_{\rm prec}$. The precession operates when the binary orbit is inclined by an angle θ with respect to the accretion disc plane. The precessing jet then subtends a cone with the half-opening angle equal to the orbit inclination $\Omega = \theta$, which we adopt from the model fit ($\Omega = 10$ deg;see Table 2). The outer disc radius $r_{\rm d}^{\rm out}$ may then be expressed as a function of the ratio between the primary BH and the total BH mass, $x_{\rm p} = M_{\rm p}/M_{\rm tot}$ (Papaloizou & Terquem 1995; Larwood 1997),

$$r_{\rm d}^{\rm out} = \left[\frac{8\pi}{3}\left(\frac{5-n}{7-2n}\right)\frac{(1+z)}{P_{\rm jet}\cos\Omega}\frac{r_{\rm ps}^3}{\sqrt{G M_{\rm tot}}}\right]^{2/3} \frac{x_{\rm p}^{1/3}}{(1-x_{\rm p})^{2/3}}, \quad (14)$$

where n is the polytropic index of the gas, $n = 3/2$ and $n = 3$ for non-relativistic and relativistic gas, respectively. Equation (14) is based on the assumption that the disc precesses as a rigid body. In order to meet this assumption, the outer disc radius needs to be smaller than the primary-secondary distance, $r_{\rm d}^{\rm out} < r_{\rm ps}$. The primary BH is also expected to be heavier than the secondary. We plot an outer disc radius $r_{\rm d}^{\rm out}$ as a function of the mass ratio $x_{\rm p}$ in Fig. 15. The suitable parameters of the binary BH are listed in Table 5. We discuss the primary-secondary distance further in Section 7. The primary-secondary distance should be between $0.001\,{\rm pc} < r_{\rm ps} < 0.1\,{\rm pc}$. A primary-secondary separation smaller than 0.001 pc would yield a

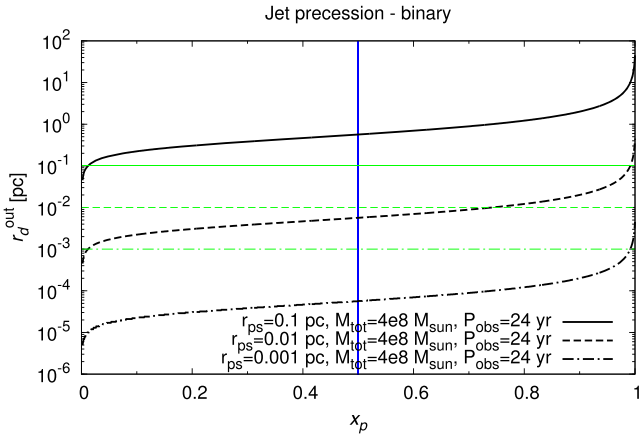

Figure 15. The function of the outer radius of a precessing disc $r_{\rm d}^{\rm out}$ as a function of the ratio of the mass of the primary BH to the total mass (black lines), $x_{\rm p} = M_{\rm p}/M_{\rm tot}$. The horizontal green lines represent the radius of the binary orbit. The vertical blue line stands for the ratio of 0.5. The primary BH is expected to be more massive than the secondary BH. The outer radius was calculated for the orbit inclination of 10 deg as inferred from the precession model fit (see Table2).

Table 5. Constraints on the parameters of a binary system in which an accretion disc (with non-relativistic gas) would undergo a precession with a period of $P = 24$ yr.

$r_{\rm ps}$ (pc)	$P_{\rm ps}^{\rm obs}$ (yr)	$x_{\rm p}^{\rm max}$	$M_{\rm p}^{\rm max}$ (M$_\odot$)	$M_{\rm s}^{\rm min}$ (M$_\odot$)
0.01	6.12	0.74	2.96×10^8	1.04×10^8
0.001	0.19	0.99	3.96×10^8	4×10^6

merger time-scale of only a few years. The upper limit is more physically motivated: at a distance of $r_{ps} = 0.1$ pc, the primary BH would have to be much smaller than the secondary BH in order to reach a precession period of the order of 24 yr, which is implausible.

6.4 Origin of the jet precession – in relation to jet launching

Based on the results of our analysis we propose that jet rotation and jet precession play a dominant role in the pc-scale jet of OJ287 and can explain the observed radio variability. We support the finding by Abraham (2000) that the optical emission is synchrotron emission and can be explained via the geometric processes of the jet precession as well.

As shown before, the time-scale of the jet precession can be explained by mainly two scenarios. These are either by Lense-Thirring precession or by precession due to a binary BH. For both models, parameters of the system could be determined. We calculated the parameters for the binary BH model based on the assumption that the primary BH mass is of the order of 10^8 $M_\odot$. In addition to this, we would like to discuss the most often discussed model for the OJ287 system – a $10^{10} M_\odot$ BH binary system ejecting a relativistic jet (Valtonen et al. 2016) with periodic plunging of a secondary BH through the primary accretion disc.

While we propose in this paper that the plunging of a secondary BH through the disc is not required to explain the observed optical variability we here discuss some implications of the Valtonen model which deserve further attention. In particular, we discuss three binary BH model configurations that potentially could explain the observational findings and their consequences with regard to the BP- (Blandford & Payne 1982) and BZ- (Blandford & Znajek 1977) jet launching models.

6.4.1 *Jet launching in binary BHs*

According to Valtonen et al. (2016), the primary BH is surrounded by an accretion disc that is penetrated twice per orbit by the secondary BH along its trajectory around the primary. The accretion disc structure is locally heavily disturbed, but local disturbances may be advected along the disc. Thus, they may reach different azimuthal locations following the Keplerian rotation, or also the inner disc radii advected with the accreted material. Jet launching may happen in two modes. Either by the BZ process of jet ejection from the corotating BH magnetosphere, or the BP mechanism of magnetocentrifugally accelerated disc winds launched from the very inner parts of the accretion disc.

In principle, if the disc perturbance that was initiated by the secondary BH reaches the jet launching area of the accretion disc, the jet acceleration would be disturbed, resulting in e.g. a variation in the mass loading of the local field strength, which would both lead to a change in the dynamics of the jet (part) that is launched from that area. The jet disturbances are supposed to follow the orbital time-scale although there will be a delay, depending on the advection time-scale from the secondary plunge region to the jet launching region. Note, however, that there might be a problem with this model. The orbital radius of the binary orbit is estimated to 0.056 pc, corresponding to about 33 Schwarzschild radii of the primary BH. On the other hand, although the jet launching region of the disc is thought to be very close to the BH, just by energetic arguments, jets are also thought to be ejected rather un-collimated and collimate further up from the launching point. That would imply that the orbit of the secondary BH is INSIDE the jet of the BP-jet. We believe that if this is the case, the jet would not be able to survive the impact of the secondary BH.

A second option is that the jet we see is only generated by the BZ process (also in the previous Section 6.4.1 there could be a jet component launched as BZ, however, we have discussed only the disc jet). Thus, considering our arguments against the disc jet scenario, the BZ jet scenario is more likely. Here, the jet stream will not be disturbed by the secondary BH directly. The accretion stream may be affected and may itself impact the mass loading of the BZ jet (by a periodic change of the radiation field of by actual mass transfer into the region close to the BH horizon).

6.4.2 *Jet direction and precession*

A variation of the jet direction may arise from various effects in the binary system. Considering jet launching as a disc wind (BP), jet precession can be expected if the BH spin axis and the accretion disc angular momentum axis are misaligned (Liu & Wu 2002; Caproni et al. 2004). This process has been confirmed by numerical simulations (Nelson & Papaloizou 2000). Recent simulations by Polko & McKinney (2017) investigate the interaction of the Lense-Thirring and electromagnetic forces on the alignment of a misaligned disc. Considering a BZ jet launching from a rotating BH, the case seems less clear. Tidal interaction between the two BHs may well lead to the precession of to BHs rotational axes. Subsequently, the BZ jet of the primary BH will precess as well. Precession of a supermassive BH and its jet has been indicated for 3C84 (Dunn, Fabian & Sanders 2006). These authors explain their data by a binary BH or by a warped disc, the time-scales derived (as well as the observed precession period) is about 10^6–10^7 yr and much larger than for our source.

Pizzolato & Soker (2005) compare bipolar planetary nebulae and the bubbles observed in clusters. They discuss two possible mechanisms which could cause the observed precession that were applied by Dunn et al. (2006) to NGC 1275. The two mechanisms are a binary BH at the centre could cause the precession of the disc of the primary BH (Katz 1997), and a disc instability that could warp the disc and cause the observed precession as well (Pringle 1997).

Following Pringle (1997) (equation 4.11),we estimate the precession time-scale

$$P_{\rm prec} \simeq 2 \times 10^7 \,{\rm yr} \times \alpha_{\rm vis}^{-1} \frac{M}{10^{10}\,{\rm M}_\odot}, \tag{15}$$

assuming a typical Shakura & Sunyaev (1973) viscosity α-parameter $\boldsymbol{\alpha_{\rm vis}}$.

On the other hand, for the binary model (Katz 1997) the typical time-scale is

$$P_{\rm prec} \simeq 10^6 \,{\rm yr} \left(\frac{M}{10^{10}\,{\rm M}_\odot}\right)^{\frac{1}{2}} \left(\frac{d}{10^{19}{\rm cm}}\right)^{3} \left(\frac{r_d^{\rm out}}{10^{18}{\rm cm}}\right)^{\frac{-3}{2}} \frac{(1+q)^{\frac{1}{2}}}{q\cos\theta} \tag{16}$$

with d being the separation between the components for a circular orbit, $r_d^{\rm out}$ the outer disc radius and θ the angle between the orbital plane and the disc plane, $q = (M_2/M_1)$, with M_1 the mass of the accreting BH and M_2 the mass of the secondary BH. $M = M_1 + M_2$ is the total mass of the binary system.

Applying the precession equation for the binary model for our orbital radius $d = 1.7 \times 10^{17}$ cm (instead of 10^{19}cm), we derive a precession period for our system a factor of 10^6 smaller than in Dunn

et al. (2006), thus about some years. This would indeed be of the order of our findings for the time-scale of the precession. Applying the estimate based on Pringle (1997) in equation (15), we see that the derived time-scale is too long (10^7 yr). We thus exclude precession of a single BH for the origin of the jet precession. However, as discussed previously, we cannot rule out disc precession.

6.4.3 Circum-binary disc

The third model scenario emerges when considering the close orbit of the secondary BH. That is the scenario of a circumstellar disc for which we assume that the binary BHs have cleaned up the disc material within their orbit. Thus, the inner radius of the circum-binary disc will be comparable to the orbital radius of the secondary BH. The inner disc may be tidally disturbed, leading to coronal flares and sub-structure in the very inner disc. Apart from the direct influence of the secondary BH, tidal effects may lead to disc warping and to subsequent jet precession. It is interesting to note that due to the disc jet launching area being further way from the minimum of the gravitational potential; in this case, we expect jets that are energetically weaker. It is known not only from model estimates but also from numerical simulations that magnetohydrodynamic (MHD) disc jets usually gain a kinetic energy that is comparable with the potential energy at the launching point. Thus, comparing a jet launching radius of say 3–10R_s in case of the Valtonen model (Valtonen et al. 2016), the jet would now be launched from a radius of 30–50R_s of the primary BH.

6.5 Circum-binary discs and mini-discs

Another explanation for the periodicities detected for OJ287 can be found in the framework of the circum-binary disc and mini-discs that can form around individual BHs in the BH binaries (Goicovic et al. 2016). The circum-binary disc can form when a massive cloud approaches the binary system, typically with a large enough impact parameter (with the pericentre distance $\approx 3R_{\rm bin}$, where $R_{\rm bin}$ is the binary radius), or when the cloud falls towards the binary in a counter-aligned way for a range of impact parameters. Goicovic et al. (2016) found that the stable and prominent mini-discs around each BH only form when the cloud falls towards the binary on an aligned orbit (in the orbital plane of the binary and corotating with the binary). These mini-discs are slightly misaligned with respect to each other as well as with respect to the binary orbital plane, which leads to the discs both 'wobbling' on a period of about half of the binary period, $P_{\rm w} = 0.5 P_{\rm bin}$, and precession (Bate et al. 2000). The precession period is $P_{\rm prec} = 20 P_{\rm bin}$ for the fiducial parameters of Goicovic et al. (2016), resulting in a ratio of $P_{\rm prec}/P_{\rm w} \approx 40$. The observed ratio between the jet precession period and the jet rotation period for OJ287 is ∼20. That ratio is achieved in this framework for an equal mass binary with mini-discs extending to half of the binary separation. While it is not straightforward to link the jet rotation/precession to the mini-disc dynamics, the arguments above show that binary systems and gas dynamics associated with them offer dynamical mechanisms to explain longer and shorter periodicities found for OJ287 and other blazars and especially the tight connection between them.

7 NOTES ON THE GRAVITATIONAL EMISSION FROM A BINARY BH

The system of two supermassive BHs will emit gravitational waves, and as a consequence, the orbit of the binary will progressively shrink and the orbital period will shorten until the merger event. The merger time-scale, which represents the time from an initial orbit radius $a_{\rm init}$ until the system merges, can be expressed as (according to Shapiro & Teukolsky 1983)

$$t_{\rm merge} = 3.65 \times 10^5 \left(\frac{a_{\rm init}}{0.01\,{\rm pc}}\right)^4 \left(\frac{M_{\rm tot}}{4\times10^8\,{\rm M}_\odot}\right)^{-3} \left(\frac{x_{\rm p}}{0.5}\right)^{-1} \times \left(\frac{x_{\rm s}}{0.5}\right)^{-1} {\rm yr}. \quad (17)$$

The relation given in equation (17) is sensitive on the initial radius, not so much the mass ratios $x_{\rm p}$ and $x_{\rm s}$ of the primary and secondary BH, respectively. It shows that the larger distance given in Table 5, $r_{\rm ps} = 0.01$ pc, is more plausible, since it gives the merger time-scale of $t_{\rm merge} \sim 10^5$ yr, whereas the smaller distance $r_{\rm ps} = 0.001$ pc yields $t_{\rm merge} \sim 36.5$ yr, which is highly unlikely given the long-term monitoring of OJ287. Taking the maximum mass for the primary in Table 5 for the distance of the components $r_{\rm ps} = 0.01$ pc, $M_{\rm p} = 3 \times 10^8\,{\rm M}_\odot$, we can express the distance in terms of the Schwarzschild radii, $r_{\rm ps} \approx 350\, M_8^{-1}\, r_{\rm s}$, where $M_8 \equiv M_{\rm p}/(3\times10^8\,{\rm M}_\odot)$, which is comparable to the binary model of (Liu & Wu 2002). However, in our model the disc is inside the orbit of the secondary BH, so the secondary does not pass through an accretion disc.

Given the maximum mass ratio of the primary BH, $x_{\rm p}^{\rm max} = 0.74$, a small core shift would be expected due to the non-negligible mass ratio. During one (observed) period of $P_{\rm ps}^{\rm obs} = 6.12$ yr, the overall linear shift would be $2x_{\rm s}r_{\rm ps} \approx 2 \times 0.26 \times 0.01$ pc $= 0.0052$ pc, which corresponds to $\sim 7 \times 10^{-4}$ mas. Since it is much smaller than the VLBI beam-size, such a small shift cannot be detected currently. An in-spiraling SMBBH would reveal itself in gravitational wave emission which would be in the frequency range detectable by the pulsar timing array. According to Babak et al. (2016), a system below a chirp mass of $10^{10}\,{\rm M}_\odot$ cannot be ruled out. Should the binary nature be confirmed, this system would likely be among the thousands of contributors to the stochastic gravitational wave background.

8 ORIGIN OF THE JET ROTATION AND THE PHYSICS OF THE JET COMPONENTS

Moving jet components, which separate with apparent superluminal motion in the range of 4–10c from the core region are generally seen in the pc-scale jets of AGN. This has been confirmed in many surveys, e.g. Britzen et al. (2008) and Lister et al. (2009). *Stationary* jet features have been observed in several BL Lac objects: e.g. 1803+784 (Britzen et al. 2010b) and 0735+178 (Britzen et al. 2010a). Recently, Jorstad et al. (2017) presented a nice discussion of the properties of stationary jet features in gamma-bright AGN. The physical nature of these components is still being debated. For OJ287, we find evidence for at least three stationary jet features. A characteristic property of these so-called stationary components is that although they remain at similar core distances for time-scales as long as a decade or longer, they reveal motion perpendicular to the jet axis. For OJ287, we find that these peculiar jet features trace the jet rotation and precession in the sky. The feature closest to the core (**a**) at a core separation of about 0.2 mas is brighter and more prominently visible in the data compared to the other two stationary components. In the following, we discuss possible physical explanations for these features.

8.1 Is component a the jet nozzle?

A possible explanation of the stationary feature **a** could be that of a precessing jet nozzle. Of the stationary features discussed above, component **a** that is closest to the core, shows the most evidence for being stationary concerning a radial motion. However, Figs 4(c) and 5(b) indicate a change in position angle that can clearly be translated in an azimuthal motion. A possible explanation of this feature is that it represents the precessing jet nozzle of OJ287. In this picture, the jet is launched as a steady outflow from a disc or the BH magnetosphere. Due to the stationary character of the outflow, no radial motion can be detected as we measure outflow velocity by motion of substructure. At some point, the innermost stationary outflow develops substructures. These could be due to the usual jet instabilities that are considered in order to explain the generation of the jet knots we observe. It could be a change in the gravitational potential, similar to what we seem to observe in *HST*-1 (a prominent feature in the jet of M87). Note that the jet of OJ287 is highly inclined. The radial position of component **a** of 0.3 mas corresponds to 1.5 pc. The presence of a stationary jet nozzle is in good agreement with recent MHD simulations of jet formation. Porth & Fendt (2010) and Porth et al. (2011) have performed relativistic MHD simulations of jet formation. Under symmetric conditions, these outflows enter a steady state. They move with relativistic speed, but are smoothly structured with no substructure that may show a (observable) pattern speed. The 3D GR-MHD simulations of McKinney & Blandford (2009) also find stable jets for opening angles of about 10 deg, although 3D modes evolve that perturb the large-scale alignment of the jet to some extent. The authors in particular mention that relativistic jets are roughly stable structures that can reach up to the region where external shocks may happen (at the interface between the jet and the ambient medium).

We believe that a slight precession of the jet source (either due to a rotating BH or the surrounding accretion disc) would lead to a precession of the jet nozzle as well. For a large precession angle, the 3D effects would be expected to destroy a steady outflow (e.g. Tchekhovskoy, Narayan & McKinney 2011; Liska et al. 2018; Sheikhezami & Fendt 2018).

We apply the inclination angle derived from our velocity data to estimate the geometry of the jet precession cone. For the following, we consider an angle of $i \simeq 7^\circ$, just between the values of 5 and 10 degrees that are suggested by our data. For the jet nozzle that we identify with the stationary component **a**, a de-projected length from the origin of 0.3 /tan i= 2.5 mas follows. Together with a 0.2 mas precession orbit (see the circle in Fig. 5, top) this indicates a full opening angle of the precession cone of $\simeq 4.6^\circ$ on the 12 pc-scale. This value nicely fits with the presumed precession on larger scales. From Fig. 2 (left) we derive a precession orbit of 1 mas at a (projected) distance of 2 mas. This translates into a de-projected length of $\simeq$16 mas and a full precession cone opening angle of 3.6 deg on the 72 pc-scale.

8.2 Is there a spine-sheath structure of the jet?

One drawback of the explanation above is, however, that these stationary components appear in several BL Lac objects and that they do not seem to be restricted to the immediate vicinity of the core. In 1803+784, most of the jet components are stationary features and their stationarity has been monitored in at least two decades of observations, e.g. Britzen et al. (2010b) and Kun et al. (2017). A precessing nozzle could explain the existence of one stationary feature. The appearance of several of these peculiar jet phenomena in the jet of OJ287, however, requires a different or an additional physical origin. A number of theoretical works and numerical simulations suggest that stationary jet features may correspond to internal recollimation shocks (e.g. Gómez et al. 1995, 1997; Cawthorne 2006; Fromm, Fuhrmann & Perucho 2015; Mizuno et al. 2015; Martí, Perucho & Gómez 2016). While this could in principle explain the existence of a pattern of such stationary features, we have some doubts that components **a**, **b**, and **c** can actually be explained as recollimation shocks. Note that we find two distinct types of components – fast moving features away from the core and those stationary components that seem to move perpendicular to the jet axis. We find it unlikely that these fast moving features could *survive* a recollimation shock representing the stationary components. To our knowledge, all simulations so far considering recollimation shocks have been performed with one outflow component only. In a recollimation shock, the shock is oriented inclined to the jet propagation direction. We believe that the latter is a highly instable configuration that potentially destroys the large-scale jet structure. In fact, we are not aware of any 3D jet simulations proving the stability of recollimation shocks, while 2D simulations indeed show stable and even steady recollimation shocks (see e.g. Komissarov & Falle 1998; Bodo & Tavecchio 2018). 2D jet simulations (e.g. Yozuke et al. 2015) seem to be capable of re-producing recollimation shocks or a series of recollimation shocks fairly well. However, extending 2D jet simulations to 3D can reduce the inherent symmetry of these calculations which can result in the production of far fewer recollimation shocks (N. MacDonald, private communication). Marscher (2009) explains that bright features in blazar jets which either are stationary or move at sub-luminal apparent speeds can in straight jets be produced by recollimation shocks or instabilities. Since OJ287 is not a straight jet, this might not be applicable. Cohen et al. (2014) find that BL Lac contains a permanent quasi-stationary feature in addition with several moving features. These moving features seem to emanate from the quasi-stationary feature. Cohen et al. (2014) explain that moving shocks are generated at a recollimation shock. The findings for BL Lac seem to differ from ours for OJ287 since we observe several stationary features. It is therefore still unclear, how both features could coexist. The word stationary is the generally used term but might be misleading since motion is detected perpendicular to the jet axis and with slow apparent speeds away from the core (for **a**). It is unclear whether recollimation shocks can reproduce this kind of motion. Thus, while recollimation shocks may be applied to reproduce the stationary pattern in other AGN, for OJ287 the model of recollimation shocks seems not sufficient to explain the variety in the jet kinematics.

A model for a spine-sheath structure in the context of astrophysical jet phenomenology has been proposed by several authors (e.g. Sol, Pelletier & Asséo 1989; Celotti, Ghisellini & Chiaberge 2001; Ghisellini, Tavecchio & Chiaberge 2005; Tavecchio & Ghisellini 2008; D'arcangelo et al. 2009; Xie et al. 2012; Mimica et al. 2015). According to these authors, most jets consist of two different regions. A low-density, fast-moving inner region which is called the jet spine. This part of the jet is thought to emerge from a region very close to the BH. A second denser and slower moving outer region is called the jet sheath. This part of the jet is thought to emerge from the inner accretion disc. Numerical simulations of accretion near BHs have shown that radial structures emerge, e.g. Porth & Fendt (2010). An observation of a possible spine has been presented for the M87 jet by Hada (2017) in 15 GHz observations obtained with the VLBA and the Jansky Array in December 2015, which, according to the authors, requires further studies. Spine-sheath po-

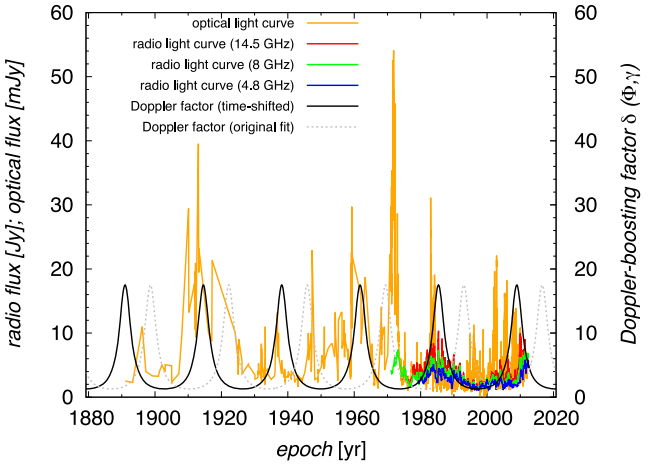

Figure 16. To visualize the relation between the optical and radio variability mentioned in the text, we show a superposition of the Doppler factor (time-shifted and calculated), the radio light-curves (4.8, 8, and 14.5 GHz), and the optical data.

larization structures have been observed in AGN jets (e.g. Gabuzda, Reichstein & O'Neill 2014). However, so far and to our knowledge, the combined spine-sheath jet structure has not been verified by observations in total intensity yet but this spine-sheath model might explain our observations. **C1–C12** show the properties based on the simulations and theoretical models and might coincide with the spine of the jet. In addition, the stationary (rotating) features might represent the sheath of the jet.

9 CONCLUSIONS

In this paper, we resolve some of the still outstanding questions related to the physical nature of the radio variability of OJ287 and the origin and dynamics of its jet. We also offer an alternative explanation for the origin of the historic optical variability. In the following, we present our conclusions.

9.1 A precessing and nutating pc-scale jet

Several investigations of the pc-scale radio jet have aimed at understanding the kinematical properties of the jet (see Section1.3). The dominant effect visible in the here presented VLBA data are that of a wandering jet in the *xy*-plane in the sky. This is most likely the result of a *precessing* jet. It is difficult to determine the precession time-scale precisely, since several cycles of the precession observed with VLBI would be required to determine the orbit with statistical significance. We model the precession and derive a time-scale of 24 ± 2 yr. This time-scale is independently confirmed by our analysis of the VLBA data. We seem to observe a full orbit and from this determine a time-scale of about 22 yr. This is roughly twice the time-scale of the dominant variability in the optical regime (of the order of about 12 yr, see Fig. 16). We suggest that the optical variability is related to this precessing motion of the radio jet and that the optical emission is synchrotron emission as well. Detailed modelling is in preparation and will be published in a forthcoming paper.

Picking one phase of the precession (where the jet remains at a similar position in the sky), the next important effect we see in the data is that of a *rotation*. The jet ridge line seems to follow the direction of precession, but then changes direction for a while before it continues again in the direction of the precession. This motion could be consistent with nutation (as discussed in Section 5.1). This can be seen in Fig. 5(b) where the upward- and downward motion of four jet components **C1**–**C4** is shown. In addition, the rotation of the jet is traced by the so-called stationary features. These components **a**, **b**, and **c** remain at similar core separations but move perpendicular to the jet axis. Their general motion perpendicular to the jet axis can be seen in Fig. 4(c). In Fig. 5(b), we show the motion of **a**. On a time-scale of about 1 yr, the position angle changes significantly which is in agreement with rotation. We compare the time-scales for brightening of component **a** through all the epochs, where **a** is detectable, and find a typical yearly time-scale. A periodicity with a time-scale of about 1 yr is also found in a detailed analysis of the 14.5 GHz radio single-dish light curve (see Section 4). The time-scales both from the VLBA data analysis and from the radio light-curve analysis are remarkably similar, baring in mind that the VLBA data are less well sampled. First, modelling results presented in this paper confirm that the data are consistent with a superposition of a precession plus nutation.

Just collecting the data of one phase of the precession reveals a pattern that looks like a *helix* which can best be seen in Fig. 3(a) by looking at all the VLBI data points collected between 2006.72 and2009.82. The helix results from a superposition of apparently fast moving components moving away from the core (the standard *superluminal features*) and apparently slow moving components (in the direction along the jet) that remain at similar core separations – but – move perpendicular to the jet axis. These latter *'stationary'* components trace the rotation (and precession) of the jet (Fig. 4c). Valtonen & Pihajoki (2013) proposed that the quasi-periodic nature of the optical light curve arises from a helical jet being observed from a small and varying viewing angle. They assume that the viewing angle variation is taken to be in tune with the binary orbital motion. However, their model does not explain the mm- and cm-radio jet observations. They claim that they are explained as being due to jet wobble at much larger (100 parsec scale) distances from the core. In this paper, we show that the jet indeed is a helix, as proposed by Valtonen & Pihajoki (2013). However, and quite in contrast to what is mentioned by Valtonen & Pihajoki (2013) the 15 GHz-jet is a helix and not wobbling at all. The jet-kinematics and -dynamics are well defined in geometrical terms. Our results most likely also discard the result of erratic jet wobbling found by Agudo et al. (2012), although we present results obtained at 15 GHz and Agudo et al. studied the jet in 43 GHz observations. We discuss several possible physical models that could explain the jet rotation, e.g. jet nozzle, spine-sheath structure, and nutation of the jet. Similarities to the X-ray binary SS433 are striking and based on the modelling presented in Section5.1, we conclude that nutation is the most likely scenario to explain our observations.

9.2 The origin of the precession

The mass of the BH of OJ287 has been independently determined in observations. Based on the observations and the application of the well-known BH mass relations, a value of $4\times 10^8\,M_\odot$ has been derived. Based on this mass estimate, we discuss several possible scenarios to explain the observed jet precession. Jet precession could be caused by a wobbling disc or a binary BH. Both the Lense-Thirring precession and the precession due to a binary companion can explain the observed precession time-scales. The precession time-scale for a binary BH scenario however seems more reasonable. Our findings are consistent with a mass of $10^8\,M_\odot$, which can correspond to the mass of a single BH or the total mass of the

binary. A massive BH of 10^{10} $M_\odot$ seems not required to explain the observed phenomena and time-scales. We nevertheless discuss the SMBBH model of Valtonen et al. with a primary mass of 10^{10} $M_\odot$.

9.3 Jet rotation and precession might cause radio and optical variability

The physical origin of the radio variability of AGN has often been attributed to the accretion phenomenon. Matter is being accreted and part of this matter is ejected into the jet and appears as a jet component - this is a short summary of the generally accepted paradigm. We here show that the radio variability in OJ287 originates in the geometry of the system – the rotating jet, most likely nutation, determines the time-scale of the rapid radio variability. The longer time-scale variability seems to originate in the precession of the jet. We thus explain the radio variability in OJ287 in terms of deterministic, geometric processes. It seems feasible that the observed variability in the radio and optical regime can be attributed solely to geometrical effects – a precessing and nutating jet with accompanying viewing angle changes and consequent Doppler beaming variations. As suggested by Abraham (2000) and discussed before (Section 5.2), we assume that both radio and optical emissions are synchrotron radiation.

OJ287 is a prototypical object. It is thus possible and likely that our findings have implications for the jets of BL Lac objects or even AGN in general. This will significantly change our understanding of jet component motion, jet launching, radio variability, and the accretion process.

Detailed modelling of the known jet kinematics is in preparation.

ACKNOWLEDGEMENTS

The authors thank both anonymous referees for carefully reading the manuscript and for many helpful suggestions that significantly improved the paper. We are thankful to P. Falke, P. Biermann, S. Komossa, D. Champion, V. M. Patiño-Álvarez, J. Roland, and N. Marchili for very helpful and insightful discussions. The help by K. Gabányi is greatly appreciated. O. Kurtanidze acknowledges financial support by the Shota Rustaveli National Science Foundation under contract FR/217554/16. Support for this work was provided by NSF grants AST-0909218 and AST-1412615 and the Levine-Leichtman Family Foundation. M. Zajacek is grateful for the financial support of the SFB956 "Conditions and Impact of Star-formation" (sub-project A2- "Conditions for Star Formation in Nearby AGN and QSO Hosts") based at the Universities of Cologne and Bonn, and the MPIfR. This research has made use of data from the MOJAVE data base that is maintained by the MOJAVE team (Lister et al. 2009). The National Radio Astronomy Observatory is a facility of the National Science Foundation operated under cooperative agreement by Associated Universities, Inc. This research was supported in part by NASA Fermi Guest Investigator awards NNX09AU16G, NNX10AP16G, NNX11AO13G, and NNX13AP18G, and by a series of grants from the NSF, most recently AST-0607523, which made the long-term UMRAO programme possible. Additional support for the operation of UMRAO was provided by the University of Michigan.

REFERENCES

Abraham Z., 2000, A&A, 355, 915
Agudo I., Marscher A. P., Jorstad S. G., Gómez J. L., Perucho M., Piner B. G., Rioja M., Dodson R., 2012, ApJ, 747, 63
Babak S. et al., 2016, MNRAS, 455, 1665
Bate M. R., Bonnell I. A., Clarke C. J., Lubow S. H., Ogilvie G. I., Pringle J. E., Tout C. A., 2000, MNRAS, 317, 773
Bessel M. S., Castelli F., Plez B., 1998, A&A, 333, 231
Bettoni D., Falomo R., Fasano G., Govoni F., Salvo M., Scarpa R., 2001, A&A, 380, 471
Blandford R. D., Payne D. G., 1982, MNRAS, 199, 883
Blandford R. D., Znajek R. L., 1977, MNRAS, 179, 433
Bodo G., Tavecchio F., 2018, A&A, 609, 122
Britzen S. et al., 2008, A&A, 484, 119
Britzen S. et al., 2010a, A&A, 515, 105
Britzen S. et al., 2010b, A&A, 511, 57
Caproni A., Abraham Z., 2004a, ApJ, 602, 625
Caproni A., Abraham Z., 2004b, MNRAS, 349, 1218
Caproni A., Mosquera Cuesta H. J., Abraham Z., 2004, ApJ, 616, 99
Cawthorne T. V., 2006, MNRAS, 367, 851
Celotti A., Ghisellini G., Chiaberge M., 2001, MNRAS, 321, L1
Cohen M. H., 2017, Galaxies, 5, 12
Cohen M. H. et al., 2014, ApJ, 787, 151
D'arcangelo F. D. et al., 2009, ApJ, 697, 985
Donskykh G., 2016, Baltic Astron., 25, 237
Dunn R. J. H., Fabian A. C., Sanders J. S., 2006, MNRAS, 366, 758
Eckart A. et al., 2017, Found. Phys., 47, 553
Efron B., 1979, Annal. Stat., 7, 1
Eracleous M., Livio M., Halpern J. P., Storchi-Bergmann T., 1995, ApJ, 438, 610
Fiorucci M., Tosti G., 1996, A&AS, 116, 403
Fromm C. M., Fuhrmann L., Perucho M., 2015, A&A, 580, 94
Gabuzda D. C., Cawthorne T. V., 1996, MNRAS, 283, 759
Gabuzda D. C., Wardle J. F. C., Roberts D. H., 1989, ApJ, 336, 59
Gabuzda D. C., Reichstein A., O'Neill E. L., 2014, MNRAS, 444, 172
Gebhardt K. et al., 2000, ApJ, 539, L13
Ghisellini G., Tavecchio F., Chiaberge M., 2005, A&A, 432, 401
Goicovic F. G., Cuadra J., Sesana A., Stasyszyn F., Amaro-Seoane P., Tanaka T. L., 2016, MNRAS, 455, 1989
Gómez J. L., Martí J. M. A., Marscher A. P., Ibanez J. M. A., Marcaide J. M., 1995, ApJ, 449, 19
Gómez J. L., Martí J. M., Marscher A. P., Ibáñez J. M., Alberdi A., 1997, ApJ, 482, 33
Hada K., 2017, Galaxies, 5, 2
Heidt J. et al., 1999, A&A, 352, 11
Hodgson J. A. et al., 2017, A&A, 597, 80
Hora J. L. et al., 2014, ApJ, 793, 120
Hovatta T., Nieppola E., Tornikoski M., Valtaoja E., Aller M. F., Aller H. D., 2008, A&A, 485, 51
Hovatta T. et al., 2014, MNRAS, 439, 690
Hughes P. A., Aller H. D., Aller M. F., 1998, ApJ, 503, 662
Jorstad S. G., et al., 2017, ApJS
Katz J. I., 1997, ApJ, 478, 527
King A., 2016, MNRAS, 456, L109
King A. R., Pringle J. E., Livio M., 2007, MNRAS, 376, 1740
Komissarov S. S., Falle S. A. E. G., 1998, MNRAS, 297, 1087
Kun E., Karouzos M., Gabanyi K. E., Britzen S., Kurtanidze O., Gergely L. A., 2018, MNRAS, in press
Larwood J. D., 1997, MNRAS, 290, 490
Lehto H. J., Valtonen M. J., 1996, ApJ, 460, 207
Liska M., Hesp C., Tchekhovskoy A., Ingram A., van der Klis M., Markoff S., 2018, MNRAS, 474, 81
Lister M. L., Homan D. C., Kadler M., Kellermann K. I., Kovalev Y. Y., Ros E., Savolainen T., Zensus J. A., 2009, ApJ, 696, 22
Lister M. L. et al., 2013, AJ, 146, 120
Liu F. K., Wu X.-B., 2002, A&A, 388, L48
Lu J. -F., 1992, Acta Astrophys. Sin., 12, 133
Magorrian J. et al., 1998, AJ, 115, 2285
Marscher A., 2009, Lect. Notes Phys., 794
Martí J. M., Perucho M., Gómez J. L., 2016, ApJ, 831, 163
McKinney J. C., Blandford R. D., 2009, MNRAS, 394, 126
McLure R. J., Dunlop J. S., 2002, MNRAS, 331, 795

Merritt D., Ferrarese L., 2001a, MNRAS, 320, L30
Merritt D., Ferrarese L., 2001b, ApJ, 547, 140
Mimica P., Giannios D., Metzger B. D., Aloy M. A., 2015, MNRAS, 450, 2824
Mizuno Y., Gómez J. L., Nishikawa K., Meli A., Hardee P. E., Rezzolla L., 2015, ApJ, 809, 38
Monceau-Baroux R., Porth O., Meliani Z., Keppens R., 2014, A&A, 561, A30
Nelson R. P., Papaloizou J. C. B., 2000, MNRAS, 315, 570
Papaloizou J. C. B., Terquem C., 1995, MNRAS, 274, 987
Pashchenko I., 2017, MNRAS, submitted
Pizzolato F., Soker N., 2005, Adv. Space Res., 36, 762
Plotkin R. M., Markoff S., Trager S. C., Anderson S. F., 2011, MNRAS, 413, 805
Polko P., McKinney J. C., 2017, MNRAS, 464, 2660
Porth O., Fendt C., 2010, ApJ, 709, 1100
Porth O., Fendt C., Meliani Z., Vaidya B., 2011, ApJ, 737, 42
Pringle J. E., 1996, MNRAS, 281, 357
Pringle J. E., 1997, MNRAS, 292, 136
Roberts D. H., Gabuzda D. C., Wardle J. F. C., 1987, ApJ, 323, 536
Shakura N. I., Sunyaev R. A., 1973, A&A, 24, 337
Shapiro S. L., Teukolsky S. A., 1983, Black Holes, White Dwarfs, and Neutron Stars: The Physics of Compact Objects, Wiley-Interscience, New York
Sheikhezami S., Fendt C., 2018, ApJ
Shepherd M. C., 1997, in Hunt G., Payne H. E., eds. ASP Conf. Ser. Vol. 125, Astronomical Data Analysis Software and Systems VI, Astron. Soc. Pac., San Francisco, p. 501
Sillanpää A., Teerikorpi P., Haarala S., Korhonen T., Efimov I. S., Shakhovskoi N. M., 1985, A&A, 147, 67
Sillanpää A., Haarala S., Valtonen M. J., Sundelius B., Byrd G. G., 1988, ApJ, 325, 628
Soltan M., Hasinger G., Egger R., Snowden S., Truemper J., 1996, A&A, 305, 17
Sol H., Pelletier G., Asséo E., 1989, MNRAS, 237, 411
Stella L., Possenti A., 2009, Space Sci. Rev., 148, 105
Stella L., Vietri M., 1998, ApJ, 492, 59
Stickel M., Fried J. W., Kühr H., 1989, A&AS, 80, 103
Storchi-Bergmann T., Eracleous M., Teresa Ruiz M. et al., 1997, ApJ, 489, 87
Storchi-Bergmann T. et al., 2003, ApJ, 598, 956
Sundelius B, Wahde M., Lehto H. J., Valtonen M. J., 1996, in Miller H. R., Webb J. R., Noble J. C. eds. ASP Conf. Ser. Vol. 110, Blazar Continuum Variability. Astron. Soc. Pac., San Francisco, p. 99
Sundelius B., Wahde M., Lehto H. J., Valtonen M. J., 1997, ApJ, 484, 180
Takalo L., 1994, Vistas Astron., 38, 77
Tateyama C. E., 2013, ApJS, 205, 15
Tateyama C. E., Kingham K. A., 2004, ApJ, 608, 149
Tateyama C. E., Kingham K. A., Kaufmann P., Piner B. G., Botti L. C. L., de Lucena A. M. P., 1999, ApJ, 520, 627
Tavecchio F., Ghisellini G., 2008, MNRAS, 385, L98
Tchekhovskoy A., Narayan R., McKinney J. C., 2011, MNRAS, 418, 79
Timmer J., Koenig M., 1995, A&A, 300, 707
Valtaoja E., 1996, in Miller H. R., Webb J. R., Noble J. C., eds, Astronomical Society of the Pacific Conference Series 110, Florida Internatial University, Florida
Valtonen M. J., Lehto H. J., 1997, ApJ, 481, L5
Valtonen M., Pihajoki P., 2013, A&A, 557, 28
Valtonen M. J., Wiik K., 2012, MNRAS, 421, 1861
Valtonen M. J. et al., 2010, CeMDA, 106, 235
Valtonen M. J., Ciprini S., Lehto H. J., 2012, MNRAS, 427, 77
Valtonen M. J. et al., 2016, ApJ, 819, L37
VanderPlas J. T., 2018, ApJS, 236, 16
Vicente L., Charlot P., Sol H., 1996, A&A, 312, 727
Witzel G., Eckart A., Bremer M. et al., 2012, ApJS, 203, 18
Witzel G. et al., 2018, submitted
Wright S. C., McHardy I. M. M., Abraham R. G., 1998, MNRAS, 295, 799
Xie W., Lei W. H., Zou Y. C., Wang D.-X., Wu Q., Wang J.-Z., 2012, Res. Astron. Astrophys., 12, 817
Yanny B., Jannuzi B. T., Impey C., 1997, ApJ, 484, L113
Mizuno Y., Gomey J. L., Nishikawa K.-I., Meli A., Hardee P. E., Rezzolla L., 2015, ApJ, 809, 38

SUPPORTING INFORMATION

Supplementary data are available at *MNRAS* online.

Appendix A. The maps and modelfit results.
Appendix B. Table of the modelfit results.

Please note: Oxford University Press is not responsible for the content or functionality of any supporting materials supplied by the authors. Any queries (other than missing material) should be directed to the corresponding author for the article.

APPENDIX A: THE MAPS & MODELFIT RESULTS

Figs A1–A8 are available online.

APPENDIX B: TABLE OF THE MODELFIT RESULTS

Table B1. The parameters derived by fitting Gaussian components to the data. *F* denotes for the flux-density, *X* for the *x*-coordinate, *Y* for the *y*-coordinate, M.A. for the major axis of the component. The last column lists the identification. The full table is available online.

Epoch	*F* (Jy)	*X* (mas)	*Y* (mas)	M.A. (mas)	Id
1995.270	0.795 ± 0.002	0.000 ± 0.000	0.000 ± 0.000	0.10 ± 0.02	k
1995.270	0.195 ± 0.002	−0.268 ± 0.002	−0.031 ± 0.002	0.10 ± 0.02	a
1995.270	0.130 ± 0.005	−0.914 ± 0.008	−0.069 ± 0.003	0.27 ± 0.01	C1
1995.270	0.163 ± 0.005	−1.279 ± 0.008	−0.009 ± 0.003	0.39 ± 0.01	
1995.270	0.033 ± 0.002	−3.238 ± 0.150	−1.047 ± 0.168	2.43 ± 0.16	
1995.840	1.417 ± 0.005	0.000 ± 0.000	0.000 ± 0.000	0.10 ± 0.02	k
1995.840	0.725 ± 0.005	−0.229 ± 0.001	−0.010 ± 0.001	0.10 ± 0.02	a
1995.840	0.135 ± 0.001	−1.297 ± 0.004	0.011 ± 0.003	0.10 ± 0.02	
1995.840	0.020 ± 0.001	−1.825 ± 0.023	−0.201 ± 0.081	0.10 ± 0.02	c

This paper has been typeset from a TEX/LATEX file prepared by the author.